Doctorate Dissertation

博士論文

Anion photoelectron spectroscopy and ion mobility mass spectrometry on chemically-synthesized gold clusters in gas phase

(化学的に合成された金クラスターの気相中における

負イオン光電子分光とイオン移動度質量分析)

A Dissertation Submitted for Degree of Doctor of Philosophy
December 2018

平成 30 年 12 月博士（理学）申請

Department of Chemistry, Graduate School of Science,
The University of Tokyo

東京大学大学院理学系研究科化学専攻

Keisuke Hirata
平田圭祐

Abstract

Ligand (L)-protected gold clusters with atomically-defined sizes, $[Au_xL_y]^z$, provide us with an ideal platform to study size-dependent evolution of structures and properties of gold in nanoscale. Geometric and electronic structures of these chemically-synthesized Au clusters have been revealed by single-crystal X-ray diffraction, X-ray and UV-vis absorption spectroscopy, cyclic voltammetry and so on. In contrast, experimental probes in the gas phase further give us complementary and precious information on intrinsic physical properties and elementary excitation and relaxation processes without perturbation from the surrounding environment. For example, photoelectron spectroscopy (PES) and photodissociation mass spectrometry (PDMS) determine the electron affinity and probe photo-induced relaxation processes including photodissociation and photodetachment. Ion mobility mass spectrometry (IMMS) allows us to determine collision cross section and to monitor collision-induced structural isomerization processes of $[Au_xL_y]^z$ in the electronically ground state.

In Chapter 1, I overview the experimental probes of geometric and electronic structures of protected metal clusters in the gas phase. I briefly summarize the chemistry of bare clusters and chemically-synthesized Au clusters.

In Chapter 2, I probed the electronic structure of a prototypical thiolate-protected Au cluster, $[Au_{25}(SR)_{18}]^-$, using anion PES and PDMS. I determined adiabatic electron affinity of $[Au_{25}(SR)_{18}]^0$ and vertical detachment energy of $[Au_{25}(SR)_{18}]^-$ for the first time. Selective photoexcitation at 266 nm to an electronically excited state results in indirect emission of thermionic electrons. This is ascribed to the promotion of internal conversion by retardation of nuclear motion toward dissociation.

In Chapter 3, I conducted IMMS on $[PdAu_8(PPh_3)_8]^{2+}$ and $[Au_9(PPh_3)_8]^{3+}$ introduced

into the gas phase by electrospray ionization (ESI). Upon collisional activation by buffer gas, the electrosprayed $[PdAu_8(PPh_3)_8]^{2+}$ and $[Au_9(PPh_3)_8]^{3+}$ were converted to smaller structures. The results suggest that the ligand layer with disordered motif in dispersion is retained during desolvation process by ESI.

In Chapter 4, I summarize the thesis and describe future prospects.

Contents

Chapter 1.

General introduction

1.1 Metal clusters

Development in nanoscience and nanotechnology in the several decades has revealed that physical and chemical properties of nanoscale materials deviate significantly from those of the corresponding bulk materials. Physical properties of nanoparticles can be quantitatively predicted by the scaling law with respect to the diameter. Specifically, the ionization potential (IP) and electron affinity (EA) of the conducting nanospheres change as a function of the diameter R according to Eqs. 1.1 and 1.2, respectively,

$$IP = WF + \frac{\alpha e^2}{R} \tag{1.1}$$

$$EA = WF - \frac{\beta e^2}{R} \tag{1.2}$$

where WF and e represent the work function of the bulk and the elementary charge, respectively.[1,2] For example, the diameter-dependent evolutional behavior can be found in Figure 1.1 showing the energies of s and d bands of coinage metal clusters as a function of $1/R$.[3] However, when the diameter of the particle is reduced below ~2 nm, the electronic levels become quantized and their energy gaps become larger than thermal energy even at room temperature.[4] These ultrasmall metal nanoparticles consisting of 2–100 atoms are defined as metal clusters. The physicochemical properties of metal clusters do not necessarily follow the scaling law as shown in Figure 1.1. Among these metal clusters, Au clusters have been enormously investigated because they show high reactivity while they are inert in the bulk form.[5,6] As shown in Figure 1.1, the energies of bare Au clusters decreases in proportion to $1/R$ as predicted by Eq. 1.2 in a larger diameter region, but they do not follow the scaling law in the cluster regime.

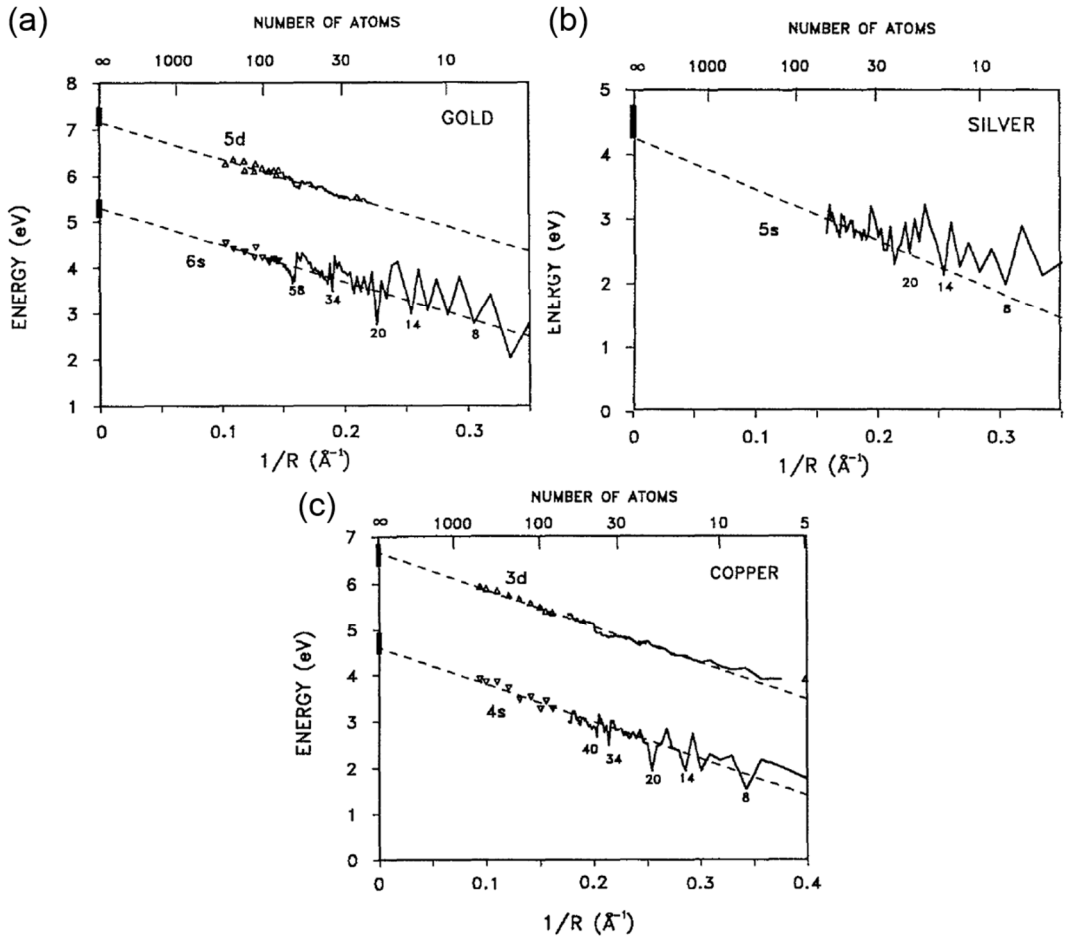

Figure 1.1 Evolution of the s and d bands of (a) Au, (b) Ag, and (c) Cu clusters as a function of the inverse of cluster radius. Solid and dotted lines correspond to the experimental data and the prediction by scaling law, respectively. Reproduced with permission from Ref. 3. Copyright 1992 American Institute of Physics.

Geometric structures of Au clusters are also significantly different from those of Au nanoparticles.[7–9] Bare Au cluster anions Au_n^- exhibit 2D sheet-like structures ($n < 13$)[8] and they evolve to hollow cages ($n = 16$–18)[9] and pyramid-like structures ($n = 19, 20$),[9] which are totally different from the face-centered cubic (fcc) structures of the Au nanoparticles. The electronic structures of Au clusters are intimately and strongly coupled with the non-fcc geometric structures.[8,9]

A metal cluster with a specific size (magic size) exhibits extraordinary stability. The

extraordinarily high stability of a magic cluster of simple metals (Au, Ag, Cu, Al) is accounted for shell closing of valence electrons accommodated in superatomic orbitals. In such bare simple metal clusters, valence electrons behave as if they were free electrons. The potential that valence electrons of a metal cluster with an isotropic shape feel is well described by a spherically symmetric Woods-Saxon potential as expressed in Eq 1.3,

$$V(r) = \frac{V_0}{1 + \exp\left(\frac{r - R}{a}\right)} \tag{1.3}$$

where V_0, R, and a correspond to the depth, radius and diffuseness of the potential well, respectively. The Woods-Saxon potential can be viewed as intermediate between the harmonic oscillator potential with a gentle potential slope and the square well potential with the steepest potential slope. The electrons in the Woods-Saxon potential are accommodated in orbitals such as 1S, 1P and 1D (Figure 1.2a).[10] Because the orbitals look similar to those of atoms in terms of symmetry, they are called superatomic orbitals (Figure 1.2b). The superatomic shell of a spherical metal cluster is closed when the valence electrons are equal to the numbers such as,

$$n = 2, 8, 18, 20, 34, 40, 58, 68, \ldots \tag{1.4}$$

For instance, clusters of simple metals such as M_n^0 (M = Au, Ag, Cu) exhibit small electron affinities at n = 8 and 20 (Figure 1.1), indicating the superatomic shell closing of M_n.

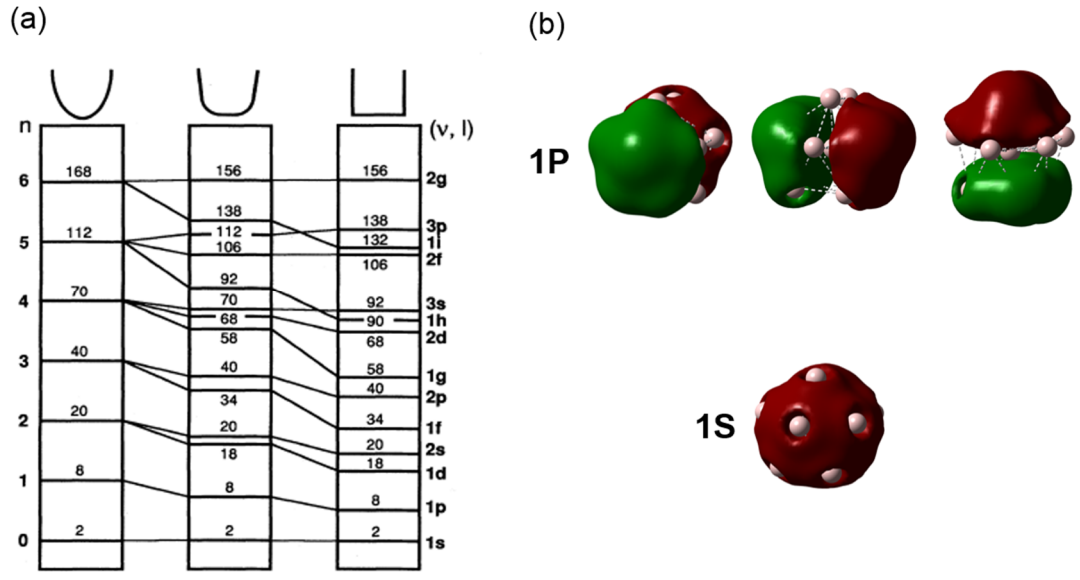

Figure 1.2 (a) Energy levels for harmonic, Woods-Saxon, and square-well potentials. (b) Typical superatomic orbitals for 1P and 1S. Reproduced with permission from Ref. 10 for (a). Copyright 1993 American Physical Society.

1.2 Ligand-protected Au clusters

Because bare metal clusters are unstable against aggregation, they cannot be treated as conventional materials. To solve the problem, clusters are stabilized by three methods: (1) stabilization by polymer, (2) immobilization on support, and (3) protection by organic ligand (L).[11] Among them, ligand protection is the most promising in terms of atomically precise synthesis. Ligand-protected Au clusters with defined compositions, $[Au_xL_y]^z$, are of particular interest because they provide us with an ideal platform to study evolutions of physical and chemical properties as a function of the number of Au atoms.[11–22] Atomically precise synthesis[11,13–18] and theoretical calculations[19–22] have deepened our understanding on structure-property correlation of the nanoscale Au materials. Historically speaking, synthetic methods of phosphine-protected Au clusters were

developed in the 1980s. In 1994, inspired by the formation of self-assembled monolayer of thiols on a flat Au surface, Brust reported that the reduction of Au-thiolate oligomers yielded small Au clusters (R <1.5 nm), indicating the first synthesis of thiolate-protected Au clusters (L = SR).[23] However, the thiolate-protected Au clusters prepared by the above method have distributions in the chemical compositions even if the synthetic conditions were well defined. In 2005, Tsukuda succeeded in synthesizing a series of glutathione (SG)-protected Au clusters, $[Au_x(SG)_y]^z$, with well-defined chemical composition using polyacrylamide gel electrophoresis (PAGE) and electrospray-ionization mass spectrometry (ESI MS) (Figure 1.3).[24]

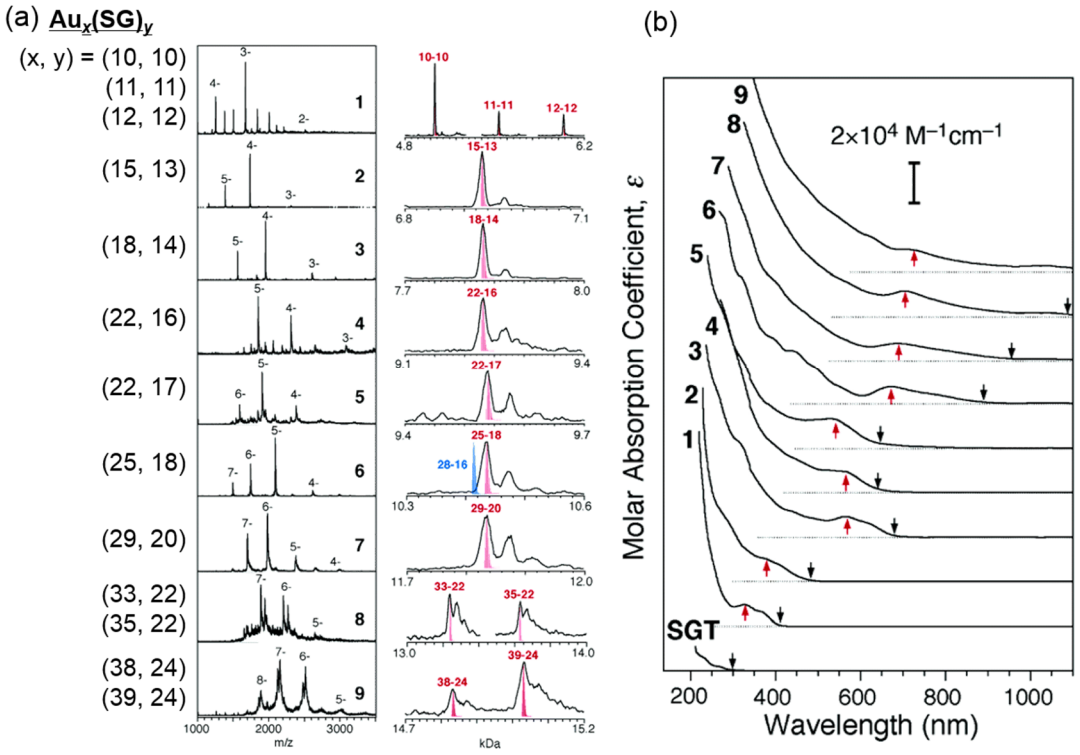

Figure 1.3 (a) ESI mass spectra and (b) UV-Vis spectra of PAGE-separated $[Au_x(SG)_y]^z$. Reproduced with permission from Ref. 24. Copyright 2005 American Chemical Society.

After the determination of specific composition of $[Au_x(SR)_y]^z$, the unique geometric structures of $[Au_xL_y]^z$ have been revealed by single-crystal X-ray diffraction

(SCXRD).[13,15,16,25–29] In 2007, Kornberg reported the crystal structure of a thiolate-protected Au cluster, $Au_{102}(p\text{MBA})_{44}$ (pMBA = p-mercaptobenzoic acid), for the first time.[25] After this groundbreaking report, the crystal structures of $[Au_{25}(PET)_{18}]^{-}$[26,27] and $Au_{38}(PET)_{24}$[28] (PET = phenylethanethiolate) were resolved (Figure 1.4). $[Au_{25}(PET)_{18}]^{-}$ has an icosahedral Au_{13} core whose surface Au atoms are completely passivated by $Au_2(PET)_3$ oligomers (Figure 1.4a). The same core motif was reported for the crystal structure of a phosphine-protected Au cluster, $[Au_{13}(dppe)_5Cl_2]^{3+}$ (dppe = 1,2-bis(diphenylphosphino) ethane) (Figure 1.4b).[29] $Au_{38}(SR)_{24}$ has a face-sharing bi-icosahedral Au_{23} core (Figure 1.4c).

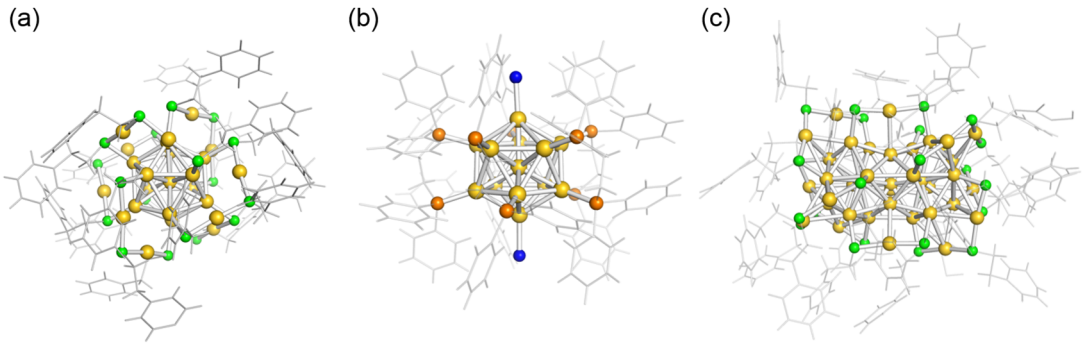

Figure 1.4 Crystal structures of (a) $[Au_{25}(PET)_{18}]^{-}$, (b) $[Au_{13}(dppe)_5Cl_2]^{3+}$, and (c) $Au_{38}(PET)_{24}$. The crystal structures are taken from Refs. 26, 29, and 28. Yellow, green, orange, and blue spheres correspond to Au, S, P, and Cl atoms, respectively. R groups are represented by wireframe.

The electronic structure of $[Au_x(SR)_y]^z$ is also understood by the superatomic concept. Häkkinen proposed a simple scheme for counting the number of valence electrons (n) in the thiolate-protected metal clusters $[Au_x(SR)_y]^z$.[19]

$$n = x - y - z \tag{1.5}$$

Superatomic shell is closed when the valence electrons are equal to the numbers listed in Eq. 1.4 when the core can be viewed as a sphere. According to Eq. 1.5, $[Au_{25}(SR)_{18}]^{-}$ has

eight (= 25–18–(–1)) electrons, which satisfies superatomic shell closing. Thus, the Au_{13} core can be viewed as a superatom with an electron configuration of $(1S)^2(1P)^6$.[19] The high stability of $[Au_{25}(SR)_{18}]^-$ is ascribed to a highly symmetrical geometry and to a closed superatomic electron configuration. The scope of atomically precise synthesis has been expanded to other coinage metal clusters.[30,31] Bakr reported the synthesis of $[Ag_{25}(SPhMe_2)_{18}]^-$, which has a similar structural motif to $[Au_{25}(SR)_{18}]^-$:[32] it has an electronically-closed, icosahedral Ag_{13} core protected by six $Au_2(SR)_3$ units. $[Ag_{29}(S_2C_6H_4)_{12}]^{3-}$ has a Ag_{13} core protected by four units of $Ag_4(S_2C_6H_4)_3$.[33] Doping of a heteroatom such as Pt and Pd to $[Ag_{25}(SPhMe_2)_{18}]^-$ was reported.[34,35]

Electronic structures of ligand-protected Au clusters have been investigated by X-ray and UV-vis absorption spectroscopy, ultrafast pump-probe spectroscopy, and cyclic voltammetry.[36–41] UV-vis absorption spectroscopy determines HOMO–LUMO gap of chemically-modified Au clusters (Figure 1.3b). The HOMO–LUMO gap can also be electrochemically determined by compensating for the charging energy.[38] Ultrafast pump-probe spectroscopy has been utilized to explore ultrafast relaxation dynamics[39] and has revealed that the lifetime of photoexcited state is much longer than that in the nanoparticles (>2 nm) and bulk,[39–41] leading to photoluminescence. Solid state X-ray photoelectron spectroscopy also provides the information on energy levels of valence bands as well as inner shell bands with respect to the Fermi level.[42]

The properties and functions of ligand-protected clusters are strongly affected by the atomic packing of the metallic core. For example, $Au_{28}(SPh^tBu)_{20}$ and $Au_{28}(Sc\text{-}C_6H_{11})_{20}$ have different isomeric Au core motifs, leading to different optical absorption profiles.[43] The modification of the ligand layer also plays a key role in the physicochemical properties such as electron transfer reactions,[44] nonlinear optical activity[45] and chiroptical

activity.[46,47] For example, the electron transfer reaction rate from $Au_{25}(SC_nH_{2n+1})_{18}$ to a carbon electrode is constant in the range of n = 12–18 owing to the formation of a bundle-like structure by the van der Waals interactions between alkyl groups.[44]

1.3 Gas-phase methods to probe geometric and electronic structures of ligand-protected Au clusters

1.3.1 Overview

As mention in Section 1.2, ESI MS has enabled mass selection of $[Au_xL_y]^z$.[24] Gas-phase experimental methods are applicable to the mass-selected ion beam of $[Au_xL_y]$. For example, anion photoelectron spectroscopy (PES) and photodissociation mass spectrometry (PDMS)[48–50] allows us to determine electron affinity (EA) and energy levels with respect to the vacuum level and to probe photo-induced relaxation processes including photodissociation and electron emission (Figure 1.5). Collision cross section (CCS), which gives the information on the shape of $[Au_xL_y]^z$, can be determined by IMMS. We are also able to monitor collision-induced isomerization in the electronically ground state by IMMS (Figure 1.5). Collision-induced dissociation mass spectrometry (CIDMS)[55–58] and surface-induced dissociation mass spectrometry (SIDMS)[59,60] have access to the fragmentation patterns of $[Au_xL_y]^z$ that may shed light on its geometric structure and bond strengths within $[Au_xL_y]^z$. Distinguished feature of gas-phase measurement is to directly probe the intrinsic electronic and geometric structures of Au nanomaterials without any perturbations from the surrounding environments. This may lead to discovery of a new photochemical phenomenon that cannot be observed due to the influence of solvents.

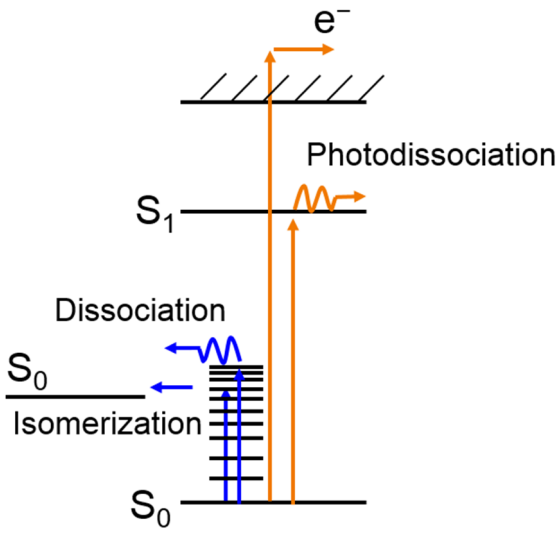

Figure 1.5 Schematic illustration of gas-phase photo-induced and collision-induced processes of $[Au_xL_y]^z$.

1.3.2 Photoelectron spectroscopy

An electron is emitted by irradiating a cluster with a photon larger than a critical energy (Eq. 1.6).

$$[Au_xL_y]^z + h\nu \rightarrow [Au_xL_y]^{z+1} + e^- \quad (1.6)$$

Photoelectron spectroscopy is a method to directly probe the electronic structures of clusters by measuring the kinetic energy of the electron detached (E_{kin}). The electron binding energy (E_b) is obtained by the following equation of energy conservation,

$$E_b = h\nu - E_{kin} \quad (1.7)$$

where $h\nu$ represents photon energy (Figure 1.6). Anion PES provides us with electron affinity of the corresponding neutral species. Magnetic-bottle type magnetic photoelectron analyzer (MBPEA) has been developed to enhance the sensitivity by collecting all photoelectrons detached omnidirectionally.[61] By using MBPEA, Smalley successfully combined MBPEA with TOFMS and observed PE spectra of Au_n^- (n = 1–

70).[3] Superatomic orbitals such as 1P and 1S will be directly probed by anion PES. Dugourd measured photodetachment yield for $[Au_{25}(SG)_{18}-6H]^{7-}$ as a function of laser wavelength.[62] However, to my best knowledge, anion PES has never been applied to $[Au_xL_y]^z$.

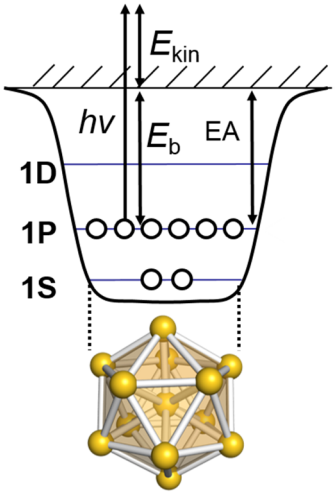

Figure 1.6 Schematic illustration of the principle of PES for ligand-protected Au clusters.

1.3.3 Photodissociation mass spectrometry

Photoexcitation leads to photodissociation as well as photodetachment (Eq. 1.8).

$$[Au_xL_y]^z + hv \rightarrow [Au_{x-m}L_{y-n}]^{z-l} + [Au_mL_n]^l \quad (1.8)$$

PDMS enables us to determine photofragment species upon photoexcitation. In 2017, PDMS was firstly applied to a ligand-protected metal clusters $[Au_{25}(p\text{MBA})_{18}]^-$.[48] Irradiation of $[Au_{25}(p\text{MBA})_{18}]^-(NH_4^+)_n$ with a 193-nm laser induce C–S bond cleavage and thus remove the ligand layer with the same size.[48]

UV absorption spectra were obtained by plotting the yield of photofragments as a function of the wavelength of a laser.[49,50] This gas-phase UV photodissociation mass spectroscopy sheds light on the absorption in the vacuum ultraviolet region that is difficult

to measure in solution phase due to the intense absorption of solvents.

1.3.4 Collision-induced dissociation mass spectrometry

Unique fragmentation patterns of $[Au_xL_y]^z$ upon collisional activation can be probed by CIDMS. It was reported that $[Au_{25}(SR)_{18}]^-$ dissociated into $[Au_{21}(SR)_{14}]^-$ as a major pathway in CID, losing $Au_4(SR)_4$ unit.[51] The generation of $[Au_{21}(SR)_{14}]^-$ was also observed in matrix-assisted laser desorption/ionization[63] and photodissociation.[48] The preferential loss of the $Au_4(SR)_4$ unit is associated with two factors: extraordinary stability of the $Au_4(SR)_4$ unit having a ring structure[64] and electronic shell closing of $[Au_{21}(SR)_{14}]^-$ with eight electrons. Recently, CID is utilized to produce size-selected bare metal clusters in the gas phase from the ligand-protected clusters. By increasing collision energy, sequential ligand loss induced the formation of bare Ag_{17}^+ clusters from $[Ag_{18}(PPh_3)_{10}H_{16}]^{2+}$.[58]

1.3.5 Surface-induced dissociation mass spectrometry

It has been demonstrated that collision of a molecule onto a solid surface can deposit large internal energy, resulting in surface-induced dissociation (SID). SID is a promising method to study the dissociation process of ligand-protected metal clusters because of the high conversion efficiency from collision energy to internal energy and short timescale (~fs) of energy conversion.[65] Efficient and ultrafast energy conversion promote fragmentation reflecting the original geometric structures. Electron transfer between a cluster and a solid surface is another important reaction in SID. Pradeep reported electron transfer from $[Ag_{11}(SG)_7]^{3-}$ $[Ag_{11}(SG)_7]^{3-}$ to a self-assembled monolayer of a fluorocarbon upon the collisional impact.[59]

1.3.6 Ion mobility mass spectrometry

With the help of ion mobility mass spectrometry (IMMS), a fundamental physical value, collision cross section (CCS), is determined. In principle, ions traverse in a cell with a pressure of several-hundred Pa propelled by an electric field (Figure 1.7). The drift velocity v_d traveling through the cell where a homogeneous static electric field E is applied is described as,

$$v_d = KE \tag{1.9}$$

where K is defined as ion mobility. The constant K is expressed as,

$$K = \frac{3ze}{16N}\left(\frac{2\pi}{\mu k_B T_{eff}}\right)^{1/2}\frac{1}{\Omega} \tag{1.10}$$

where z, e, N, μ, k_B, T_{eff} and Ω are the charge of the target cluster, the elementary charge, the number density of the buffer gas, the reduced mass of the target cluster and a buffer gas atom/molecule, the Boltzmann constant, the effective temperature of the target cluster, and the CCS, respectively. Thus, the value of Ω can be determined by measuring the drift velocity, v_d. The high pressure in the cell prohibits ions to exit the cell and hence the ion intensity is decreased. This requires highly sensitive measurement. To overcome this problem, various methods have been developed including traveling wave ion mobility mass spectrometry (TWIMMS).[66] Recently, ESI-coupled TWIMMS has been readily conducted due to a commercially available TWIM mass spectrometer (Synapt G2-HDMS, Synapt G2-Si, Waters Corp., U.K.).[51–54] In fact, ESI-coupled TWIMMS (Synapt G2-Si) is used in Chapter 3. Dass reported the first IMMS of thiolate-protected Au clusters.[51] Pradeep extended the scope to thiolate-protected Ag clusters.[52] Isomerization processes of $[Au_xL_y]^z$ has been revealed by IMMS. Johnson reported the abrupt decrease of the arrival time of $[Au_8(PPh_3)_{7-x}(PPh_2Me)_x]^{2+}$ from x = 3 to 4.[53] This behavior was attributed

to the emergence of a densely packed ligand layer of the phosphine ligands owing to dispersion interactions.

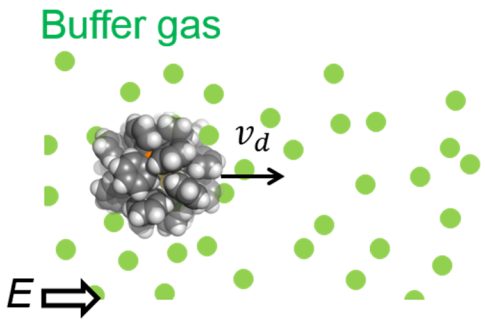

Figure 1.7 Schematic illustration of the principle of IMMS for ligand-protected Au clusters.

1.4 Aim and outline

$[Au_xL_y]^z$ provides an ideal platform to study size-dependent evolution of structures and properties of gold in nanoscale. Geometric and electronic structures of these chemically-synthesized Au clusters have been revealed by SCXRD, optical spectroscopy, voltammetry and so on. However, experimental methods in the gas phase further give us complementary and valuable information on intrinsic physical properties and elemental excitation and relaxation processes without perturbation from the surrounding environment. For example, PES and PDMS determine the electron affinity and probe photo-induced relaxation processes including dissociation and electron emission. IMMS allows us to determine CCS and to monitor collision-induced structural isomerization processes of $[Au_xL_y]^z$.

In my thesis, I experimentally probed the photo-induced and collision-induced processes of $[Au_xL_y]^z$ using PES, PDMS and IMMS. In Chapter 2, I conducted PES and PDMS of $[M_{25}(SR)_{18}]^-$ (M = Au, Ag) to determine the EAs and to probe relaxation processes upon photoexcitation. SCXRD has revealed that $[M_{25}(SR)_{18}]^-$ has an

icosahedral M_{13} core whose surface Au atoms are fully covered with $M_2(SR)_3$ oligomers. Theoretical calculations revealed that the M_{13} core can be viewed as a protected superatom with a halogen-like closed electron configuration of $(1S)^2(1P)^6$. However, important physical properties of protected superatoms such as EA remained unclear. The other remaining problem is that the research on photophysical processes was limited to relaxation dynamics of photoexcited states. Photoinduced oxidation, which is related to photostability, has not been explicitly taken into account. The motivation of this study is to determine the EAs of $[M_{25}(SR)_{18}]^-$ and to directly probe intrinsic photo-induced processes of $[M_{25}(SR)_{18}]^-$ without perturbation of solvents. In Chapter 3, I conducted IMMS of $[PdAu_8(PPh_3)_8]^{2+}$ and $[Au_9(PPh_3)_8]^{3+}$ to reveal whether their structures in the gas phase are same with those determined by SCXRD and whether the isomerization can be induced upon collisional excitation. $[Au_9(PPh_3)_8]^{3+}$ takes two isomeric core motifs while $[PdAu_8(PPh_3)_8]^{2+}$ takes only one structural motif. They have densely packed PPh_3 ligand layers due to CH–π and π–π interactions in the crystal forms. However, the structures in dispersing media would be different from those in the crystal because of the solute-solvent interactions. In this sense, isomerization not only in core motif but also in ligand layer can be expected in $[PdAu_8(PPh_3)_8]^{2+}$ and $[Au_9(PPh_3)_8]^{3+}$. In Chapter 4, I summarize the whole work and conclude future prospects.

References

1. Makov, G.; Nitzan, A.; Brus, L. E. On the Ionization Potential of Small Metal and Dielectric Particles. *J. Chem. Phys.* **1988**, *88*, 5076–5085.
2. Perdew, J. P. Energetics of Charged Metallic Particles: from Atom to Bulk Solid. *Phys. Rev. B* **1988**, *37*, 6175–6180.
3. Taylor, K. J.; Pettiette-Hall, C. L.; Cheshnovsky, O.; Smalley, R. E. Ultraviolet Photoelectron Spectra of Coinage Metal Clusters. *J. Chem. Phys.* **1992**, *96*, 3319–3329.
4. Kubo, R. Electronic Properties of Metallic Fine Particles. I. *J. Phys. Soc. Jpn.* **1962**, *17*, 975–986.
5. Bernhardt, T. M. Gas-Phase Kinetics and Catalytic Reactions of Small Silver and Gold Clusters. *Int. J. Mass Spectrom.* **2005**, *243*, 1–29.
6. Wallace, W. T.; Whetten, R. L. Coadsorption of CO and O_2 on Selected Gold Clusters: Evidence for Efficient Room-Temperature CO_2 Generation. *J. Am. Chem. Soc.* **2002**, *124*, 7499–7505.
7. Glib, S.; Weis, P.; Furche, F.; Ahlrichs, R.; Kappes, M. M. Structures of Small Gold Cluster Cations (Au_n^+, n<14): Ion Mobility Measurements versus Density Functional Calculations. *J. Chem. Phys.* **2002**, *116*, 4094–4101.
8. Häkkinen, H.; Yoon, B.; Landman, U.; Li, X.; Zhai, H.-J.; Wang, L.-S. On the Electronic and Atomic Structures of Small Au_N^- (N = 4–14) Clusters: A Photoelectron Spectroscopy and Density-Functional Study. *J. Phys. Chem. A* **2003**, *107*, 6168–6175.
9. Bulusu, S.; Li, X.; Wang, L.-S.; Zeng, X. C. Evidence of Hollow Golden Cages. *Proc. Natl. Acad. Sci.* **2006**, *103*, 8326–8330.
10. de Heer, W. A. The Physics of Simple Metal Clusters: Experimental Aspects and Simple Models. *Rev. Mod. Phys.* **1993**, *65*, 611–676.
11. Tsukuda, T. Toward an Atomic-Level Understanding of Size-Specific Properties of Protected and Stabilzied Gold Clusters *Bull. Chem. Soc. Jpn.* **2012**, *85*, 151–168.
12. Chen, S.; Ingram, R. S.; Hostetler, M. J.; Pietron, J. J.; Murray, R. W.; Schaaff, T. G.; Khoury, J. T.; Alvarez, M. M.; Whetten, R. L. Gold Nanoelectrodes of Varied Size: Transition to Molecule-Like Charging. *Science* **1998**, *280*, 2098–2101.
13. Jin, R.; Zheng, C.; Zhou, M.; Chen, Y. Atomically Precise Colloidal Metal Nanoclusters and Nanoparticles: Fundamentals and Opportunities. *Chem. Rev.* **2016**, *116*, 10346–10413.
14. Chakraborty, I.; Pradeep, T. Atomically Precise Clusters of Noble Metals: Emerging Link between Atoms and Nanoparticles. *Chem. Rev.* **2017**, *117*, 8208–8271.
15. Konishi, K. Phosphine-Coordinated Pure-Gold Clusters: Diverse Geometrical Structures and Unique Optical Properties/Responses. *Struct. Bond* **2014**, *161*, 49–86.
16. Lei, Z.; Wan, X.-K.; Yuan, S.-F.; Guan, Z.-J.; Wang, Q.-M. Alkynyl Approach toward the

Protection of Metal Nanoclusters. *Acc. Chem. Res.* **2018**, *51*, 2465–2474.

17. Yao, Q.; Chen, T.; Yuan, X.; Xie, J. Toward Total Synthesis of Thiolate-Protected Metal Nanoclusters. *Acc. Chem. Res.* **2018**, *51*, 1338–1348.
18. Sakthivel, N. A.; Dass, A. Aromatic Thiolate-Protected Series of Gold Nanomolecules and a Contrary Structural Trend in Size Evolution. *Acc. Chem. Res.* **2018**, *51*, 1774–1783.
19. Walter, M.; Akola, J.; Lopez-Acevedo, O.; Jadzinsky, P. D.; Calero, G.; Ackerson, C. J.; Whetten, R. L.; Grönbeck, H.; Häkkinen, H. A Unified View of Ligand-Protected Gold Clusters as Superatom Complexes. *Proc. Natl. Acad. Sci.* **2008**, *105*, 9157–9162.
20. Tang, Q.; Hu, G.; Fung, V.; Jiang, D. Insights into Interfaces, Stability, Electronic Properties, and Catalytic Activities of Atomically Precise Metal Nanoclusters from First Principles. *Acc. Chem. Res.* **2018**, *51*, 2793–2802.
21. Xu, W. W.; Zheng, X. C.; Gao, Y. Application of Electronic Counting Rules for Ligand-Protected Gold Nanoclusters. *Acc. Chem. Res.* **2018**, *51*, 2739–2747.
22. Aikens, C. M. Electronic and Geometric Structure, Optical Properties, and Excited State Behavior in Atomically Precise Thiolate-Stabilized Noble Metal Nanoclusters. *Acc. Chem. Res.* **2018**, *51*, 3065–3073.
23. Brust, M.; Walker, M.; Bethell, D.; Schiffrin, D. J.; Whyman, R. Synthesis of Thiol-Derivatised Gold Nanoparticles in a Two-Phase Liquid-Liquid System. *J. Chem. Soc., Chem. Commun.* **1994**, *0*, 801–802.
24. Negishi, Y.; Nobusada, K.; Tsukuda, T. Glutathione-Protected Gold Clusters Revisited: Bridging the Gap between Gold(I)-Thiolate Complexes and Thiolate-Protected Gold Nanocrystals. *J. Am. Chem. Soc.* **2005**, *127*, 5261–5270.
25. Jadzinsky, P. D.; Calero, G.; Ackerson, C. J.; Bushnell, D. A.; Kornberg, R. D. Structure of a Thiol Monolayer-Protected Gold Nanoparticle at 1.1Å Resolution. *Science* **2007**, *318*, 430–433.
26. Heaven, M. W.; Dass, A.; White, P. S.; Holt, K. M.; Murray, R. M. Crystal Structure of the Gold Nanoparticle $[N(C_8H_{17})_4][Au_{25}(SCH_2CH_2Ph)_{18}]$ *J. Am. Chem. Soc.* **2008**, *130*, 3754–3755.
27. Zhu, M.; Aikens, C. M.; Hollander, F. J.; Schatz, G. C.; Jin, R. Correlating the Crystal Structure of A Thiol-Protected Au_{25} Cluster and Optical Properties. *J. Am. Chem. Soc.* **2008**, *130*, 5883–5885.
28. Qian, H.; Eckenhoff, W. T.; Zhu, Y.; Pintauer, T.; Jin, R. Total Structure Determination of Thiolate-Protected Au_{38} Nanoparticles. *J. Am. Chem. Soc.* **2010**, *132*, 8280–8281.
29. Shichibu, Y.; Konishi, K. HCl-Induced Nuclearity Convergence in Diphosphine-Protected Ultrasmall Gold Clusters: A Novel Synthetic Route to "Magic-Number" Au_{13} Clusters. *Small* **2010**, *6*, 1216–1220.

30. Bhattarai, B.; Zaker, Y.; Atnagulov, A.; Yoon, B.; Landman, U.; Bigioni, T. P. Chemistry and Structure of Silver Molecular Nanoparticles. *Acc. Chem. Res.* **2018**, *51*, 3104–3113.
31. Ghosh, A.; Mohammed, O. F.; Bakr, O. Atomic-Level Doping of Metal Clusters. *Acc. Chem. Res.* **2018**, *51*, 3094–3103.
32. Joshi, C. P.; Bootharaju, M. S.; Alhilaly, M. J.; Bakr, O. M. $[Ag_{25}(SR)_{18}]^-$: The "Golden" Silver Nanoparticle. *J. Am. Chem. Soc.* **2015**, *137*, 11578–11581.
33. AbdulHalim, L. G.; Bootharaju, M. S.; Tang, Q.; Del Gobbo, S.; AbdulHalim, R. G.; Eddaoudi, M.; Jiang, D.-e.; Bakr, O. M. $Ag_{29}(BDT)_{12}(TPP)_4$: A Tetravalent Nanocluster. *Nanoscale* **2016**, *8*, 17333–17339.
34. Yan, J.; Su, H.; Yang, H.; Malola, S.; Lin, S.; Häkkinen, H.; Zheng, N. Total Structure and Electronic Structure Analysis of Doped Thiolated Silver $[MAg_{24}(SR)_{18}]^{2-}$ (M =Pd, Pt) Clusters. *J. Am. Chem. Soc.* **2015**, *137*, 11880–11883.
35. Bootharaju, M. S.; Sinatra, L.; Bakr, O. M. Distinct Metal-Exchange Pathways of Doped Ag_{25} Nanoclusters. *Nanoscale* **2016**, *8*, 17333–17339.
36. Jin, R. Atomically Precise Metal Nanoclusters: Stable Sizes and Optical Properties. *Nanoscale* **2015**, *7*, 1549–1565.
37. Negishi, Y.; Nakazaki, T.; Malola, S.; Takano, S.; Niihori, Y.; Kurashige, W.; Yamazoe, S.; Tsukuda, T.; Häkkinen, H. A Critical Size for Emergence of Nonbulk Electronic and Geometric Structures in Dodecanethiolate-Protected Au Clusters. *J. Am. Chem. Soc.* **2015**, *137*, 1206–1212.
38. Kwak, K.; Lee, D. Electrochemistry of Atomically Precise Metal Nanoclusters. *Acc. Chem. Res.* **2019**, *52*, 12–22.
39. Yau, S. H.; Varnavski, O.; Goodson III, T. An Ultrafast Look at Au Nanoclusters. *Acc. Chem. Res.* **2013**, *46*, 1506–1516.
40. Yi, C.; Zheng, H.; Herbert, P. J.; Chen, Y.; Jin, R. Knappenberger, Jr. Ligand- and Solvent-Dependent Electronic Relaxation Dynamics of $Au_{25}(SR)_{18}^-$ Monolayer-Protected Clusters. *J. Phys. Chem. C* **2017**, *121*, 24894–24902.
41. Kwak, K.; Thanthirige, V. D.; Pyo, K.; Lee, D.; Ramakrishna, G. Energy Gap Law for Exciton Dynamics in Gold Cluster Molecules. *J. Phys. Chem. Lett.* **2017**, *8*, 4898–4905.
42. Ohta, T.; Shibuta, M.; Tsunoyama, H.; Negishi, Y.; Eguchi, T.; Nakajima, A. Size and Structure Dependence of Electronic States in Thiolate-Protected Gold Nanoclusters of $Au_{25}(SR)_{18}$, $Au_{38}(SR)_{24}$, $Au_{144}(SR)_{60}$. *J. Phys. Chem. C* **2013**, *117*, 3674–3679.
43. Chen, Y.; Liu, C.; Tang, Q.; Zeng, C.; Higaki, T.; Das, A.; Jiang, E.-e.; Rosi, N. L.; Jin, R. Isomerism in $Au_{28}(SR)_{20}$ Nanocluster and Stable Structures. *J. Am. Chem. Soc.* **2016**, *138*, 1482–1485.
44. Antonello, S.; Arrigoni, G.; Dainese, T.; Nardi, M. D.; Parisio, G.; Perotti, L.; René, A.;

Venzo, A.; Maran, F. Electron Transfer through 3D Monolayers on Au_{25} Clusters. *ACS Nano* **2014**, *8*, 2788–2795.

45. Knoppe, S.; Verbiest, T. Resonance Enhancement of Nonlinear Optical Scattering in Monolayer-Protected Gold Clusters. *J. Am. Chem. Soc.* **2017**, *139*, 14853–14856.
46. Knoppe, S.; Bürgi, T. Chirality in Thiolate-Protected Gold Clusters. *Acc. Chem. Res.* **2014**, *47*, 1318–1326.
47. Takano, S.; Tsukuda, T. Amplification of Optical Activity of Gold Clusters by the Proximity of BINAP. *J. Phys. Chem. Lett.* **2016**, *7*, 4509–4513.
48. Black, D. M.; Crittenden, C. M.; Brodbelt, J. S.; Whetten, R. L. Ultraviolet Photodissociation of Selected Gold Clusters: Ultraefficient Unstapling and Ligand Stripping of $Au_{25}(pMBA)_{18}$ and $Au_{36}(pMBA)_{24}$. *J. Phys. Chem. Lett.* **2017**, *8*, 1283–1289.
49. Greisch, J.; Ballester-Caudet, A.; Kruppa, S. V.; Lei, Z.; Wang, Q.; Riehn, C.; Remacle, F. Gas-Phase Photoluminescence and Photodissociation of Silver-Capped Hexagold Clusters. *J. Phys. Chem. A* **2018**, *122*, 5799–5810.
50. Daly, S.; Choi, C. M.; Zavras, A.; Krstić, M.; Chirot, F.; Connell, T. U.; Williams, S. J.; Donnelly, P. S.; Antione, R.; Giuliani, A.; Bonačić-Koutecký, V.; Dugourd, P.; O'Hair, R. A.J. Gas-Phase Structural and Optical Properties of Homo- and Heterobimetallic Rhombic Dodecahedral Nanoclusters $[Ag_{14-n}Cu_n(C{\equiv}CtBu)_{12}X]^+$ (X = Cl and Br): Ion Mobility, VUV and UV Spectroscopy, and DFT Calculations. *J. Phys. Chem. C* **2017**, *121*, 10719–10727.
51. Angel, L.; Majors, L.; Dharmaratne, A.; Dass, A. Ion Mobility Mass Spectrometry of $Au_{25}(SCH_2CH_2Ph)_{18}$ Nanoclusters. *ACS Nano* **2010**, *4*, 4691–4700.
52. Baksi, A.; Ghosh, A.; Mudedla, S. K.; Chakraborty, P.; Bhat, S.; Mondal, B.; Krishnadas, K. R.; Sabramanian, V.; Pradeep, T. Isomerism in Monolayer Protected Silver Cluster Ions: An Ion Mobility-Mass Spectrometry Approach. *J. Phys. Chem. C* **2017**, *121*, 13421–13427.
53. Ligare, M. R.; Baker, E. S.; Laskin, J.; Johnson, G. E. Ligand Induced Structural Isomerism in Phosphine Coordinated Gold Clusters Revealed by Ion Mobility Mass Spectrometry. *Chem. Commun.* **2017**, *53*, 7389–7392.
54. Baksi, A.; Chakraborty, P.; Bhat, S.; Natarajan, G.; Pradeep, T. $[Au_{25}(SR)_{18}]_2^{2-}$: a Noble Metal Cluster Dimer in the Gas Phase. *Chem. Commun.* **2016**, *52*, 8397–8400.
55. Black, D. M.; Bhattarai, N.; Whetten, R. L.; Bach, S. B. H. Collision-Induced Dissociation of Monolayer Protected Clusters Au_{144} and Au_{130} in an Electrospray Time-of-Flight Mass Spectrometer. *J. Phys. Chem. A* **2014**, *118*, 10679–10687.
56. Chakraborty, P.; Baksi, A.; Khatun, E.; Nag, A.; Ghosh, A.; Pradeep, T. Dissociation of Gas Phase Ions of Atomically Precise Silver Clusters Reflects Their Solution Phase Stability. *J. Phys. Chem. C* **2017**, *121*, 10971–10981.
57. Tomihara, R.; Hirata, K.; Yamamoto, H.; Takano, S.; Koyasu, K.; Tsukdua, T. Collision-

Induced Dissociation of Undecagold Clusters Protected by Mixed Ligands $[Au_{11}(PPh_3)_8Cl_2]^+$ (X = Cl, C≡CPh). *ACS Omega* **2017**, *121*, 10971–10981.

58. Ghosh, A.; Bodiuzzaman, M.; Nag, A.; Jash, M.; Baksi, A.; Pradeep, T. Sequential Dihydrogen Desorption from Hydride-Protected Atomically Precise Silver Clusters and the Formation of Naked Clusters in the Gas Phase. *ACS Nano* **2017**, *11*, 11145–11151.
59. Baksi, A.; Harvey, S. R.; Natarajan, G.; Wysocki, V. H.; Pradeep, T. Possible Isomers in Ligand Protected Ag_{11} Cluster Ions Identified by Ion Mobility Mass Spectrometry and Fragmented by Surface Induced Dissociation. *Chem. Commun.* **2016**, *52*, 3805–3808.
60. Johnson, G. E.; Priest, T.; Laskin, J. Size-Dependent Stability toward Dissociation and Ligand Binding Energies of Phosphine Ligated Gold Cluster Ions. *Chem. Sci.* **2014**, *5*, 3275–3286.
61. Kruit, P.; Read, F. H. Magnetic Field Paralleliser for 2π Electron-Spectrometer and Electron-Image Magnifier. *J. Phys. E: Sci. Instrum.* **1983**, *16*, 313–324.
62. Hamouda, R.; Bellina, B.; Bertorelle, F.; Compagnon, I.; Antoine, R.; Broyer, M.; Rayane, D.; Dugourd, P. Electron Emission of Gas-Phase $[Au_{25}(SG)_{18}-6H]^{7-}$ Gold Cluster and Its Action Spectroscopy. *J. Phys. Chem. Lett.* **2010**, *1*, 3189–3194.
63. Dass, A.; Stevenson, A.; Dubay, G. R.; Tracy, J. B.; Murray, R. W. Nanoparticle MALDI-TOF Mass Spectrometry without Fragmentation: $Au_{25}(SCH_2CH_2Ph)_{18}$ and Mixed Monolayer $Au_{25}(SCH_2CH_2Ph)_{18-x}(L)_x$. *J. Phys. Chem. Lett.* **2010**, *1*, 3189–3194.
64. Grönbeck, H.; Walter, M.; Häkkinen, H. Theoretical Characterization of Cyclic Thiolated Gold Clusters. *J. Am. Chem. Soc.* **2006**, *128*, 10268–10275.
65. Zhou, M.; Wysocki, V. H. *Acc. Chem. Res.* **2014**, *47*, 1010–1018.
66. Shvartsburg, A. A.; Smith, R. D. Fundamentals of Traveling Wave Ion Mobility Spectrometry. *Anal. Chem.* **2008**, *80*, 9689–9699.

Chapter 2.

Anion photoelectron spectroscopy of $[M_{25}(SR)_{18}]^-$ (M = Au, Ag)

Hirata, K.; Yamashita, K.; Muramatsu, S.; Takano, S.; Ohshimo, K.; Azuma, T.; Nakanishi, R.; Nagata, T.; Yamazoe, S.; Koyasu, K.; Tsukuda, T. *Nanoscale* **2017**, *9*, 13409–13412.

Hirata, K.; Kim, K.; Nakamura, K.; Kitazawa, H.; Hayashi, S.; Koyasu, K.; Tsukuda, T. *J. Phys. Chem. C* submitted.

2.1 Introduction

Coinage metal clusters protected by organic ligands $M_x(L)_y$ (M = Au, Ag; L = thiolate, phosphine, alkynyl) have broadened the scope of materials science owing to their size-specific novel properties.[1–6] Atomically precise synthesis[2–10] and theoretical calculations[11–14] have promoted our understanding on how the structures and properties evolve as a function of the number of core atoms (x) of $M_x(L)_y$. Extensive studies in the last decade revealed that they exhibit unique structures and properties that cannot be predicted by scaling laws. Single-crystal X-ray crystallography has demonstrated the formation of metallic cores with non-fcc geometries.[15–18] Optical spectroscopy and voltammetry have shown that they exhibit clear HOMO–LUMO gaps reflecting the quantized electronic structures.[19–21] Ultrafast spectroscopy has revealed that the lifetime of the photoexcited state is much longer than that in the nanoparticles (>2 nm) and bulk,[22–24] leading to photoluminescence. Theoretical studies have shown that the valence

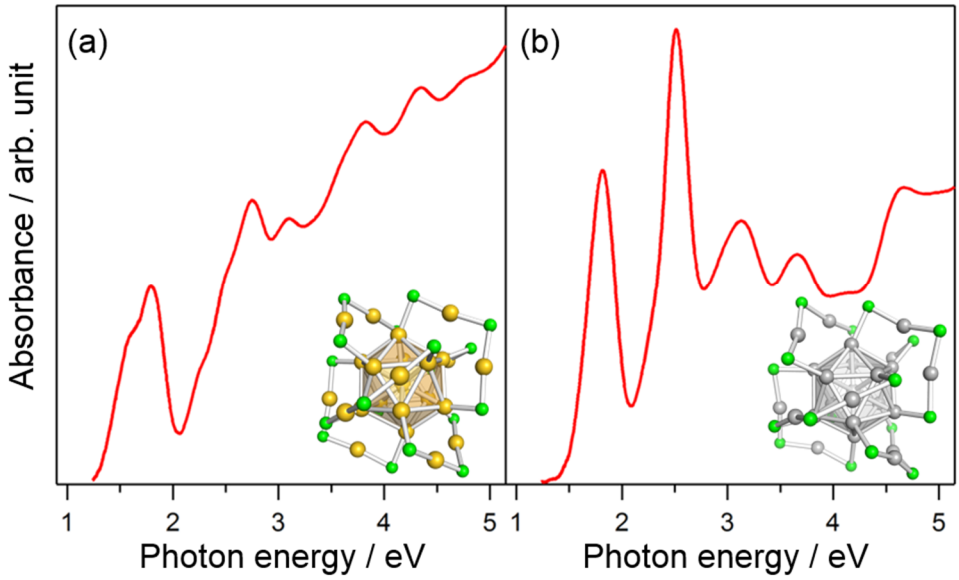

Figure 2.1 Optical absorption spectra of (a) $[Au_{25}(SC_2H_4Ph)_{18}]^-$ and (b) $[Ag_{25}(SPhMe_2)_{18}]^-$. Insets show the crystal structures taken from Refs 16 and 27. Orange, gray and green colors indicate Au, Ag, and S atoms, respectively. The R group is omitted for clarity.

electrons are accommodated into the superatomic orbitals (1S, 1P, 1D, …) formed in the metallic core.[11,14]

Thiolate (RS)-protected $[M_{25}(SR)_{18}]^-$ (M = Au, Ag) are representative of the systems that have been studied in the greatest depth.[25–27] They have an icosahedral M_{13} core with surface M atoms fully bonded to six bidentate $M_2(SR)_3$ oligomers (Figure 2.1).[16,17,27] The M_{13} core can be viewed as a superatom with a closed superatomic electron configuration of $(1S)^2(1P)^6$.[11] The lowest energy bands in the UV-Vis spectra (Figure 2.1) are assigned to the electronic transition from HOMO (1P) to LUMO (1D).[14,17] Electronic transitions within the metallic core as well as between the core and ligands are involved in photoabsorption in the higher energy region.[28] Photophysical processes have been studied using ultrafast spectroscopy to gain a fundamental understanding of the relaxation dynamics of the photoexcited states as well as to promote applications for chemical detection,[29] biotherapy[30] and photocatalysis,[31] and photodynamic therapy.[32] However, photoinduced oxidation, which may be directly related to the photostability, has not been explicitly considered.

2.2 Methods

2.2.1 Synthesis

2.2.1.1 $[Au_{25}(SC_{12}H_{25})_{18}]^-TOA^+$

$[Au_{25}(SR)_{18}]^-(TOA)^+$ was synthesized according to a method[16] previously reported with modifications. A 300 mL Erlenmeyer flask was charged with 523 mg of $HAuCl_4 \cdot 4H_2O$ (1.27 mmol), 779 mg of TOABr (1.43 mmol), and a Teflon-coated magnetic stir bar. 70 mL of THF was added to the flask and stirring was started at room temperature yielding a dark-red homogeneous solution. Then, 3.04 mL of $C_{12}H_{25}SH$ (12.7

mmol) was added dropwise to the solution under constant stirring and the stirring was continued for 1.5 h. At this stage, the color of the solution slowly turned to faint yellow. The stirring was set to vigorous (~750 rpm) and a freshly prepared $NaBH_4$ solution (480 mg; 12.7 mmol in 10 mL of cold water) was added to the solution all at once. Violent gas evolution occurred and the black colored solution was stirred at the same speed for 16 h. The THF layer was filtered through a paper filter and the volatiles were evaporated giving a black oil covered with water. The oil was precipitated by methanol and the precipitate was collected by centrifugation. This methanol washing procedure was repeated five times and the precipitate was dried *in vacuo*. The dried product was extracted by a minimum amount of dichloromethane and the solution was precipitated by methanol containing TOABr (2 mg/mL). The precipitates were washed by methanol two more times. Acetone (~50 mL) was added to the precipitate and the solution was centrifuged. The supernatant was evaporated to dryness and to the sticky black solid was added acetone (~50 mL). The solution was centrifuged and the supernatant was evaporated to dryness. The black residue was dissolved in a minimum amount of dichloromethane and the solution was concentrated by Ar flow. Finally, the solid was dried *in vacuo* at room temperature, giving 118.9 mg (26% yield based on Au) of the title compound as a brown powder.

2.2.1.2 $[Au_{25}(SC_2H_4Ph)_{18}]^-TOA^+$

A 1 L round-bottomed flask was charged with 2.08 g of $HAuCl_4 \cdot 4H_2O$ (5.08 mmol), 3.12 g of tetraoctylammonium bromide (TOABr) (1.43 mmol), and Teflon-coated magnetic stir bar. 140 mL of THF was added to the flask, and stirring (100 rpm) was started at room temperature yielding a dark-red homogeneous solution. 3.6 mL of

HSC_2H_4Ph (26.8 mmol) was added dropwise to the solution under stirring and the stirring was kept for ~12 h. At this stage, the color of the solution slowly turned into colorless. A freshly prepared $NaBH_4$ solution (1.9 g; 50 mmol in 50 mL of ice-cold water) was added to the solution all at once. Gas evolution occurred and the black colored solution was stirred at the same speed for 60 h. The THF layer was filtered through a paper filter and the volatiles were evaporated giving a black oil covered with water. The oil was precipitated by methanol and the precipitate was collected by centrifugation. This methanol washing procedure was repeated five times and the precipitate was dried *in vacuo*. The dried product was extracted by a minimum amount of dichloromethane and the solution was precipitated by methanol which contains TOABr (1 mg/mL). The precipitates was washed by methanol one more time. Toluene (20 mL) was added to the precipitate and the solution was centrifuged. The supernatant was filtered through a cotton plug in a 200 mL pear-shaped flask and 150 mL of *n*-pentane was carefully layered on the toluene solution. After standing overnight, black crystals were deposited on the bottom of the flask. Faint yellow supernatant was decanted and the crystals were washed by *n*-pentane for two times. Finally, the crystals were dried *in vacuo* at room temperature giving 464 mg (29 % yield based on Au) of the title compound as black needles.

2.2.1.3 $[Ag_{25}(SPhMe_2)_{18}]^-(PPh_4)^+$

$[Ag_{25}(SPhMe_2)_{18}]^-(PPh_4)^+$ was synthesized according to a method[27] previously reported with modifications in the purification step. A 30 mL glass vial was charged with 38.7 mg of $AgNO_3$ (0.228 mmol) dissolved in 2 mL methanol with the aid of sonication. Stirring (280 rpm) was started at room temperature, and 117 μL of 2,4-dimethylbenzenethiol (0.87 mmol) was added to the vial, yielding a yellow precipitate.

After 18 mL of dichloromethane (DCM) was added, the solution was kept in the room temperature for 20 minutes with constant stirring. Then, 5.9 mg of tetraphenylphosphonium bromide (PPh_4Br) (0.014 mmol) dissolved in 0.5 mL methanol was added to the solution. The solution was cooled in an ice-bath (0 C°) and kept for 30 minutes. Next, a freshly prepared $NaBH_4$ solution (14.9 mg; 0.394 mmol in 5 mL of ice-cold water) was added to the solution dropwise over a period of 10 minutes under vigorous stirring. The color of the solution turned into dark brown. After the mixture was kept stirring in an ice-bath for 6 h, the mixture was kept standing in a freezer (–20 C°). The purification process was modified from the original procedure. The DCM layer was separated from the aqueous layer and was filtered to remove an insoluble black precipitate. The filtrate was concentrated to 5 mL by evaporating solvents and was added dropwise to 40 mL of methanol. After 16 h stirring (1200 rpm) in room temperature, a dark brown precipitate was formed. The precipitate was collected by filtration and washed with methanol three times. Then, the precipitate was dissolved in 40 mL of DCM to remove a yellow precipitate. The filtrate was concentrated to 5 mL and added dropwise to 40 mL of methanol. The product was soluble in this step probably because of the removal of byproducts in the previous step. After 5 minutes of stirring, the solution was filtrated and the filtrate was evaporated. The dried sample was again dissolved in 5 mL of DCM and added dropwise to 40 mL of hexane. The brown precipitate formed after 5 minutes of stirring was collected by filtration and washed with hexane three times. The precipitate was dissolved in 10 mL of DCM, layered with 20 mL of hexane, and was left in a freezer (5 Cº). Brown needle-like crystals were formed after one week. Typical yield: 6.5 mg (13 % based on Ag).

2.2.2 Overview of experimental apparatus

The experimental apparatus used in the study is composed of an electrospray ionization (ESI) source, a time-of-flight mass spectrometer (TOFMS) and a magnetic-bottle type photoelectron analyzer (MBPEA) (Figures 2.2a). The flight path lengths of the TOFMS and MBPEA are 1.66 and 1.91 m, respectively. Acetonitrile/toluene (1/1, v/v) dispersion of $[Au_{25}(SR)_{18}]^-$ or DCM dispersion of $[Ag_{25}(SR)_{18}]^-$ (1–3 mg/mL) was electrosprayed at a flow rate of 1.5 μL min^{-1} to a capillary resistively heated in the range of 110–120 °C. $[M_{25}(SR)_{18}]^-$ ions thus desolvated were accelerated up to 12.8 keV by a pulsed voltage (200 μs, 10 Hz) applied to Wiley–McLaren acceleration grids and were detected by the TOFMS with a typical mass resolution ($M/\Delta M$) of 600. The mass-selected beam of $[M_{25}(SR)_{18}]^-$ was irradiated with the third or fourth harmonic output of a nanosecond Nd:YAG laser (GCR-130, Spectra-Physics, U.S.). Photoelectrons emitted from $[M_{25}(SR)_{18}]^-$ were collected by the inhomogeneous magnetic field. The electron kinetic energies were determined using the MBPEA. A typical energy resolution ($E/\Delta E$) was 110 meV for an electron with a kinetic energy of 1 eV.

The PD mass spectra were obtained by irradiating the continuous beam from the ESI source containing chemically isolated clusters with the third or fourth harmonic output of a Nd:YAG laser (Quanta-Ray INDI-40, Spectra-Physics, U.S.) 1 μs before pulsed acceleration of the anions (Figure 2.2b). The photofragments produced by laser irradiation were measured by the TOFMS. PD difference mass spectrum was obtained by subtracting the mass spectrum with laser irradiation from that without laser irradiation: negative and positive peaks indicate the depletion of parent ions and generation of daughter ions, respectively.

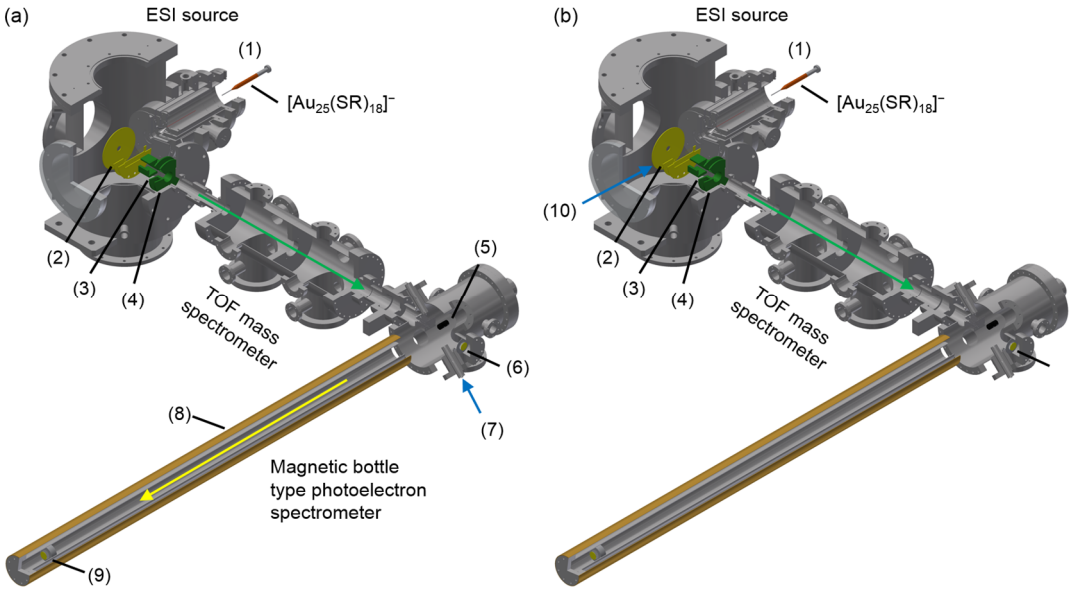

Figure 2.2 Schematic illustration of the experimental setup for (a) anion PES and (b) PDMS. (1) Syringe, (2) Wiley–McLaren type acceleration grids, (3) deflectors, (4) einzel lens, (5) permanent magnet, (6) microsphere plate, (7) photodetachment laser, (8) coil, (9) microchannel plate, and (10) photodissociation laser,. Green and yellow arrows indicate the trajectory of ions and photoelectrons, respectively.

2.3 Photoelectron spectroscopy of $[Au_{25}(SC_{12}H_{25})_{18}]^-$ at 355 nm

The purity of the sample was confirmed by ESI mass spectrometry and UV-Vis spectroscopy (Figure 2.3). Figure 2.4b shows the photoelectron spectrum of $[Au_{25}(SC_{12}H_{25})_{18}]^-$ obtained by accumulating 200,000 laser shots for six hours (21–47 mJ

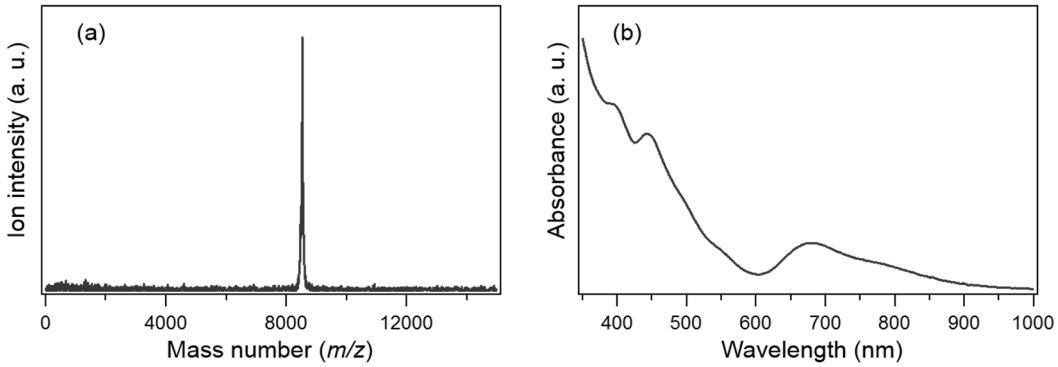

Figure 2.3 (a) ESI mass spectrum and (b) UV-Vis spectrum of $[Au_{25}(SC_{12}H_{25})_{18}]^-$.

pulse^{-1} cm^{-2}). The spectrum exhibits two bands labeled as A and B. According to the previous theoretical calculation, the HOMO of $[Au_{25}(SR)_{18}]^-$ is a 1P superatomic orbital and HOMO−1 with an Au 5d nature is located below the HOMO by 0.98 eV.[17] Therefore, band A and B are assigned to the electron detachment from the 1P superatomic orbital and that from the Au 5d orbital localized on the Au atoms, respectively. According to the valence-band X-ray PES on solid sample of $[Au_{25}(SC_{12}H_{25})_{18}]^-$,[33] band B is assigned to Au $5d_{5/2}$. However, the peak position of band B cannot be unambiguously determined at present due to limits in the energy of the photons. In the following, I focus only on band A.

The energies of the top and onset of band A, E_{top} and E_{th}, were determined to be 2.5 and 2.2 eV, respectively. Band A is not split into two due to the spin-orbit coupling in the neutral state: DFT calculations predict the splitting of 0.2 eV.[34] A schematic potential energy diagram relevant to the photoelectron detachment from $[Au_{25}(SC_{12}H_{25})_{18}]^-$ to $[Au_{25}(SC_{12}H_{25})_{18}]^0$ is shown in the inset of Figure 2.4b. Since the energy minimum structures of $[Au_{25}(SR)_{18}]^-$ and $[Au_{25}(SR)_{18}]^0$ are slightly different due to Jahn-Teller effect,[35] the photoelectron spectrum is broadened by a Frank-Condon overlap between the two states. The E_{top} value corresponds to vertical detachment energy (VDE), the energy required to remove an electron while retaining the geometrical structure. In contrast, the E_{th} value corresponds to the AEA of $[Au_{25}(SC_{12}H_{25})_{18}]^0$ (Figure 2.4b). Namely, the AEA of $[Au_{25}(SC_{12}H_{25})_{18}]^0$ was determined to be 2.2 eV. This AEA value agrees with the onset (~600 nm, ~2.1 eV) of the photodetachment yield curve of $[Au_{25}(SG)_{12}(SG'^-)_6]^-$ (SG = glutathiolate; SG'$^-$ = deprotonated form of SG).[36] The AEA values of methylthiolate-protected $[Au_{25}(SCH_3)_{18}]^0$ were predicted to be 3.0[37,28] and 3.17,[38] whereas the VDE value was calculated to be 2.81 eV.[39] The theoretical AEA and

VDE values are significantly larger than the experimental values. This is probably due to the overestimation of energy levels of open-shell $[Au_{25}(SCH_3)_{18}]^0$.

The intensity of the photodetachment laser used in this work (21–47 mJ/pulse/cm^2) was significantly higher than that used in the conventional PES experiments on metal cluster anions.[40] This is because the ion intensity of $[Au_{25}(SC_{12}H_{25})_{18}]^-$ is weak due to pulsed extraction from the continuous beam of $[Au_{25}(SC_{12}H_{25})_{18}]^-$ from the ESI source: the duty factor was only 0.2%. Under such light source conditions, there is a possibility that PES data was affected by multi-photon (most likely two-photon) processes: (i) photodetachment from the excited state populated by the 355 nm laser; (ii) photodetachment from fragments produced by the 355 nm laser. The former process is unlikely to occur given that the lifetime of the photoexcited state is very short (~200 fs upon excitation at 400 nm) compared to nanoscale laser pulses.[22] In contrast, the second process may be involved in PES measurement using an Ar-F laser (193 nm, 6.42 eV), for example, as a light source. This is because $[Au_2(SR)_3]^-$ fragment with an adiabatic electron affinity (AEA) of 4.06 eV[41] may be produced according to the photodissociation study of $[Au_{25}(p\text{MBA})_{16}(p\text{MBA'}^-)_2]^-$ (*p*MBA = *p*-mercaptobenzoic acid; *p*MBA'$^-$ = deprotonated form of *p*MBA) at 193 nm.[42] We tested the latter possibility by recording the photodissociation mass spectra of $[Au_{25}(SC_{12}H_{25})_{18}]^-$ at 355 nm (Figure 2.4a). Upon 355 nm laser irradiation, the peak of $[Au_{25}(SC_{12}H_{25})_{18}]^-$ is depleted significantly while only a small amount (<5%) of $[Au_{21}(SC_{12}H_{25})_{14}]^-$ was detected as a photofragment. This result indicates that direct electron detachment is the dominant process upon irradiation of $[Au_{25}(SC_{12}H_{25})_{18}]^-$ at 355 nm.

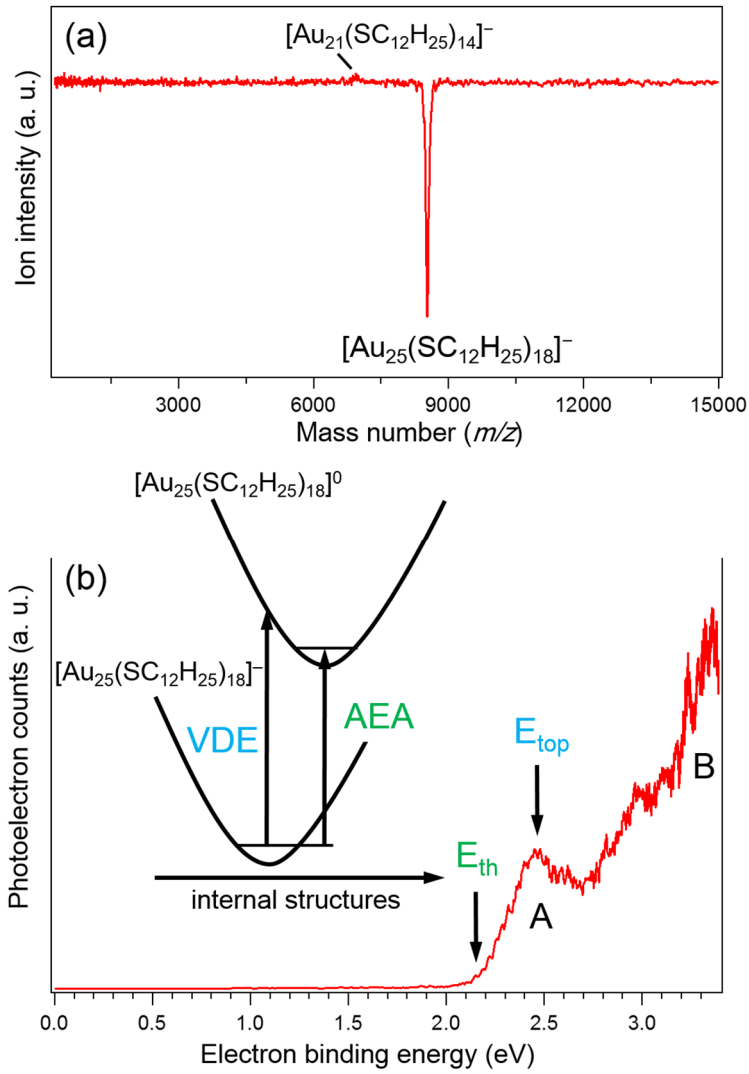

Figure 2.4 (a) Photodissociation mass spectrum and (b) photoelectron spectrum of $[Au_{25}(SC_{12}H_{25})_{18}]^-$ at 355 nm. Inset shows schematic potential energy diagram of $[Au_{25}(SC_{12}H_{25})_{18}]^-$ and $[Au_{25}(SC_{12}H_{25})_{18}]^0$.

2.4 Photo-induced thermionic emission from $[M_{25}(SR)_{18}]^-$ (M = Au, Ag)

The purity of the samples was confirmed by optical spectroscopy (Figure 2.1) and mass spectrometry (Figure 2.5). To determine the peak position of band B, anion PES of $[Au_{25}(SR)_{18}]^-$ at higher energy is necessary. I recorded the PE spectra of $[Au_{25}(SC_2H_4Ph)_{18}]^-$ and $[Ag_{25}(SPhMe_2)_{18}]^-$ both at 355 and 266 nm. Figure 2.6a shows

the PE spectrum of $[Au_{25}(SC_2H_4Ph)_{18}]^-$ recorded at 355 nm by accumulating photoelectron signals for six hours. The spectrum exhibits two bands, A and B, similar to those observed in the PE spectrum of $[Au_{25}(SC_{12}H_{25})_{18}]^-$. Bands A and B were assigned to the direct photodetachment from superatomic 1P orbitals and 5d orbitals localized on the Au atoms, as in the case of $[Au_{25}(SC_{12}H_{25})_{18}]^-$. From the onset of band A, the AEA value of $[Au_{25}(SC_2H_4Ph)_{18}]^0$ was determined to be 2.36±0.01 eV, which is close to that of $[Au_{25}(SC_{12}H_{25})_{18}]^0$ (2.2 eV). Figure 2.6b shows the PE spectrum of $[Au_{25}(SC_2H_4Ph)_{18}]^-$ recorded at 266 nm to probe the deeper electronic structure. To our surprise, the spectrum profile is completely different from that at 355 nm (Figure 2.6a) and is dominated by a new band, C, at an electron binding energy of >4.0 eV. The expanded PE spectrum at 266 nm exhibits direct photodetachment corresponding to bands A and B. These findings indicate that slow electron emission dominates over direct photodetachment upon photoirradiation of $[Au_{25}(SC_2H_4Ph)_{18}]^-$ at 266 nm. A similar phenomenon was observed in the PE spectra of $[Ag_{25}(SPhMe_2)_{18}]^-$ recorded at 355 and 266 nm, as shown in Figures 2.6d and 2.6e, respectively. Bands A′ and B′ at 355 nm were assigned to direct photodetachment from superatomic 1P orbitals and 4d orbitals localized on the Ag atoms, respectively. The AEA value was determined to be 2.02±0.02 eV. The PE spectrum at 266

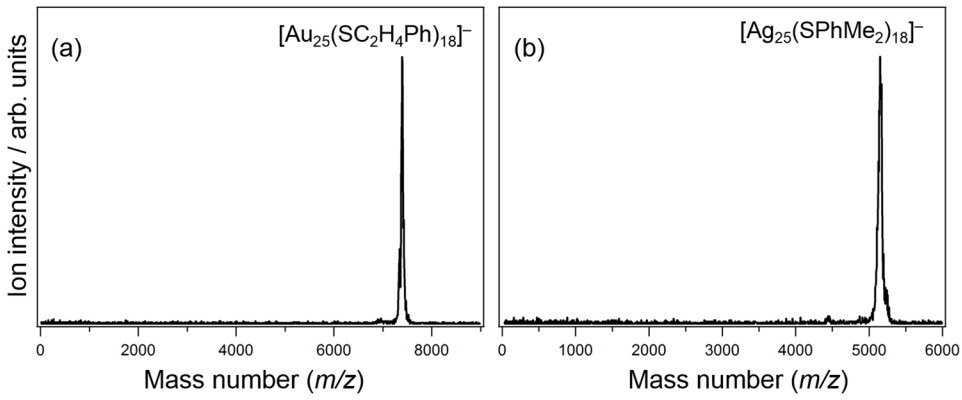

Figure 2.5 ESI mass spectra of (a) $[Au_{25}(SC_2H_4Ph)_{18}]^-$ and (b) $[Ag_{25}(SPhMe_2)_{18}]^-$.

nm was also dominated by band C′ with a low kinetic energy.

Emission of slow photoelectrons from bare metal cluster anions[43,44] and chromophores of photoactive yellow protein[45] has been observed and ascribed to thermionic emission (TE) from vibrationally excited anions. Efficient photoinduced TE was observed from cluster anions of W, Nb, and Pt having small vertical detachment energies and large vaporization energies in the corresponding bulk metal.[44] In the framework of a simple model where the absorbed photon energy is equally dissipated to vibrational internal degrees of freedom, the temperature T of the cluster anion is given by:

$$T = \frac{hv}{nk_B} \tag{2.1}$$

where hv, k_B and n represent the absorbed photon energy, the Boltzmann constant, and the number of vibrational degrees of freedom, respectively. Kinetic energy of the electrons emitted by TE follows a Boltzmann distribution and the photoelectron intensity I_{TE} is given by:

$$I_{TE} = A\exp\left(-\frac{E_{kin}}{k_B T}\right) \tag{2.2}$$

where E_{kin} indicates the electron kinetic energy.[43,44] If we assume that the absorbed energy is equally distributed to the vibrational degrees of freedom ($n = 3\times13-3 = 33$) of the Au_{13} and Ag_{13} cores, the temperature of the core is calculated to be 1.6×10^3 K according to Eq. 1. Kinetic energy distributions at 1.6×10^3 K simulated by Eq. 2.2 are shown as black dotted lines in Figures 2.6b and 2.6e. Good agreement between the simulated curves with the profiles of bands C and C′ supports the assignment to TE from the Au_{13} and Ag_{13} cores. This is in sharp contrast to the absence of TE from bare Au and Ag cluster anions.[40]

The above discussion suggests that the key to TE is the suppression of fragmentation

of cluster anions electronically excited above the electron detachment threshold. To check their robustness in the electronically excited state, the PD mass spectra of $[Au_{25}(SC_2H_4Ph)_{18}]^-$ and $[Ag_{25}(SPhMe_2)_{18}]^-$ were recorded at 266 nm. Figures 2.6c and 2.6f show typical PD mass spectra of $[Au_{25}(SC_2H_4Ph)_{18}]^-$ and $[Ag_{25}(SPhMe_2)_{18}]^-$ at 266 nm, respectively. Both sets of spectra were dominated by the depletion of the parent ions. No photofragment ions from $[Au_{25}(SC_2H_4Ph)_{18}]^-$ were observed, whereas $[Ag_{22}(SPhMe_2)_{15}]^-$ was observed as a minor fragment from $[Ag_{25}(SPhMe_2)_{18}]^-$. These results indicate that the TE is a major decay pathway of $[Au_{25}(SC_2H_4Ph)_{18}]^-$ and

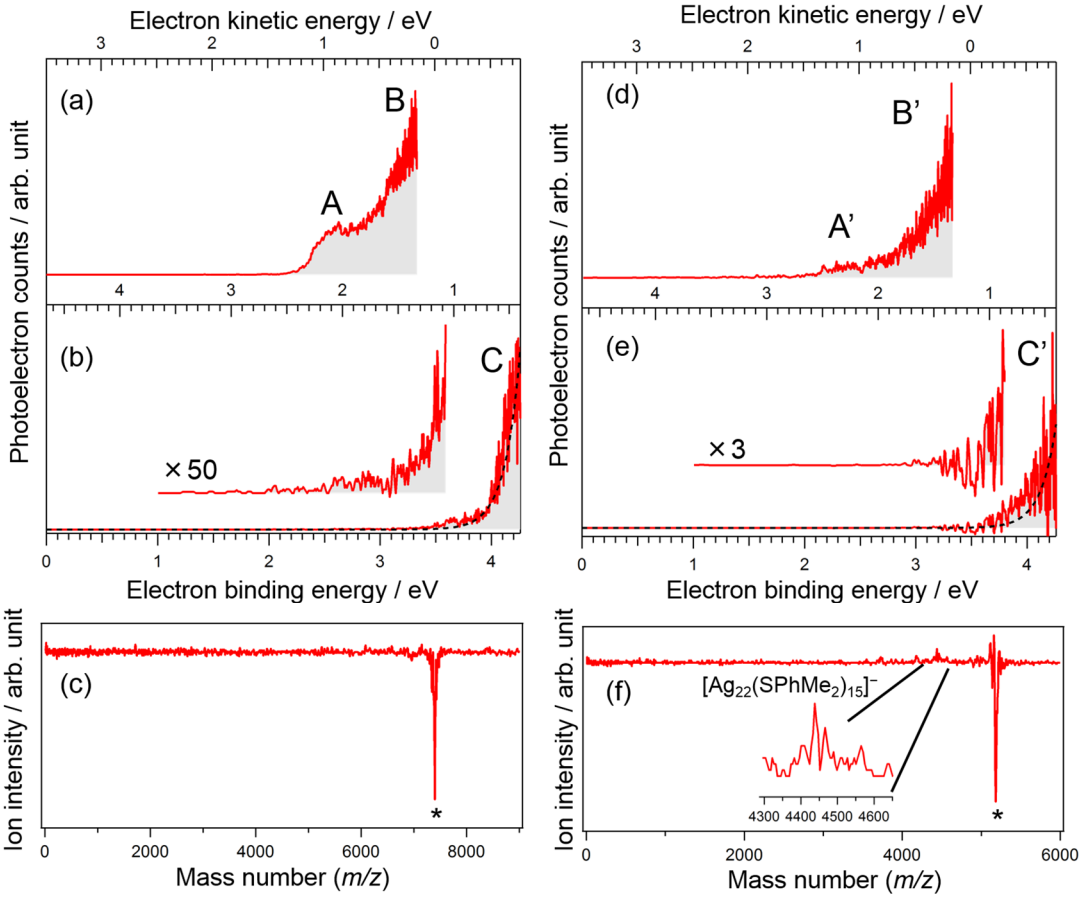

Figure 2.6 PE spectra of $[Au_{25}(SC_2H_4Ph)_{18}]^-$ at (a) 355 and (b) 266 nm and those of $[Ag_{25}(SPhMe_2)_{18}]^-$ at (d) 355 and (e) 266 nm. PD mass spectra of (c) $[Au_{25}(SC_2H_4Ph)_{18}]^-$ and (f) $[Ag_{25}(SC_2H_4Ph)_{18}]^-$ at 266 nm. Red solid and black dotted lines correspond to experimental data and simulated curves for thermionic emission of M_{13} core, respectively. The peaks with an asterisk correspond to the depletion of parent ions.

$[Ag_{25}(SPhMe_2)_{18}]^-$ photoexcited at 266 nm.

Relaxation pathways of $[M_{25}(SR)_{18}]^-$ upon photoexcitation at 266 nm are explained by a Jablonski diagram (Figure 2.7). Since photoelectron signals by direct photodetachment are much weaker than those by TE, the initial step is selective excitation of $[M_{25}(SR)_{18}]^-$ into $[M_{25}(SR)_{18}]^{-}$*, which is embedded in the photodetachment continuum (shaded area in Figure 2.7). Electronic transitions within the M_{13} core as well as metal-to-ligand transitions[28] would be involved in the electronic transitions at 266 nm. Large absorbances at 266 nm in the UV-Vis spectrum (Figure 2.1) support the selective excitation to an electronically excited state. Electronically excited $[M_{25}(SR)_{18}]^{-}$* quickly undergoes internal conversion (IC) to form vibrationally excited $[M_{25}(SR)_{18}]^-$ followed by TE leaving internal energy in the remaining neutral $[M_{25}(SR)_{18}]^0$. Photodissociation, a competing process of IC, is almost completely suppressed even though the photon energy

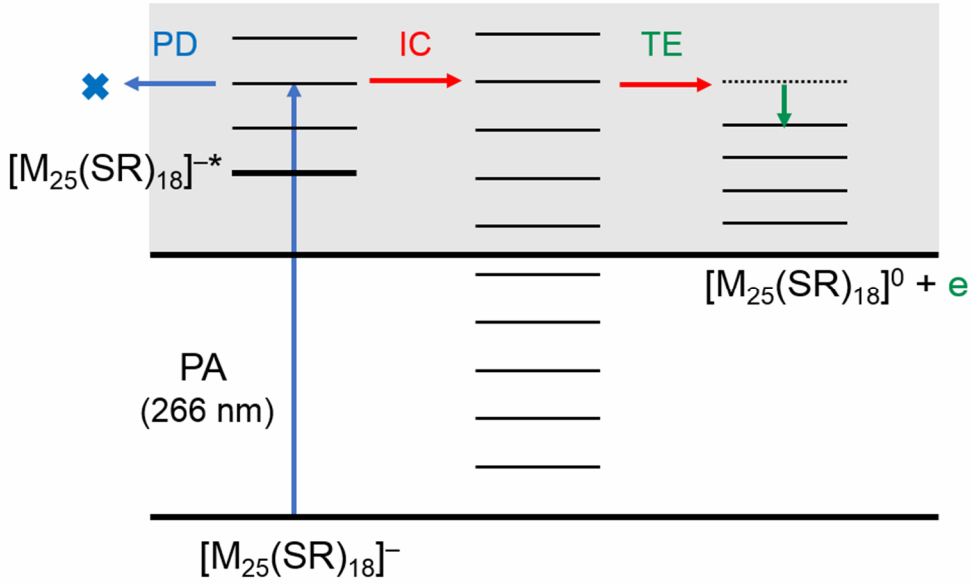

Figure 2.7 Jablonski diagram illustrating the TE pathway of $[M_{25}(SR)_{18}]^-$ following the photoexcitation at 266 nm. Horizontal lines are vibrational levels. Gray area indicates the electron detachment continuum. PA = photoabsorption; PD = photodissociation; IC = internal conversion; TE = thermionic emission.

exceeds the energy required for the dissociation into $[M_{21}(SR)_{14}]^-$ and $M_4(SR)_4$ (2.9 eV for M = Au).[46] Protection of the M_{13} core by stiff $M_2(SR)_3$ units[42] may contribute to the promotion of IC process of $[M_{25}(SR)_{18}]^{-*}$ by retarding the nuclear motion toward the dissociation.

2.5 Summary

In summary, I successfully recorded the photoelectron spectrum of $[M_{25}(SR)_{18}]^-$, a representative ligand-protected coinage cluster anion for the first time. The PE spectrum of $[Au_{25}(SC_{12}H_{25})_{18}]^-$ at 355 nm exhibits two bands that correspond to the photodetachment from the 1P superatomic orbital and Au 5d bands. The AEA and VDE values were determined to be 2.2 and 2.5 eV, respectively, indicating that theoretical calculation overestimates the AEA values probably due to overestimation of energy of open-shell neutral species. Since the solvation energy of the anionic state is generally larger than that of the neutral state, the minimum photon energy required for the electron detachment from $[Au_{25}(SC_{12}H_{25})_{18}]^-$ in organic dispersion is expected to be larger than the VDE value.

Anion PES and PDMS were conducted on thiolate-protected coinage metal clusters $[M_{25}(SR)_{18}]^-$ (M =Au, Ag) isolated in vacuum at 266 nm. $[M_{25}(SR)_{18}]^-$ underwent TE of slow electrons without direct electron detachment nor dissociation upon irradiation with 266-nm photons with an energy (4.66 eV) exceeding the electron detachment threshold energies (2.02–2.36 eV). Curve fitting analysis suggests that TE occurs from the M_{13} core with a vibrational temperature of 1.6×10^3 K. Exclusive TE from $[M_{25}(SR)_{18}]^-$ is ascribed to the selective transition to an electronically excited state embedded in the electron detachment continuum and quick IC to vibrationally excited $[M_{25}(SR)_{18}]^-$. This study

illustrates that gas-phase methods such as anion PES and PDMS provide a new opportunity to address intrinsic electronic structures and photoinduced processes of ligand-protected metal clusters without any influence from the solvents.

References

1. Chen, S.; Ingram, R. S.; Hostetler, M. J.; Pietron, J. J.; Murray, R. W.; Schaaff, T. G.; Khoury, J. T.; Alvarez, M. M.; Whetten, R. L. Gold Nanoelectrodes of Varied Size: Transition to Molecule-Like Charging. *Science* **1998**, *280*, 2098–2101.
2. Tsukuda, T.; Häkkinen, H. Protected Metal Clusters: From Fundamentals to Applications, 1st ed.; Elsevier, B. V.: Amsterdam, The Netherlands, 2015.
3. Jin, R.; Zheng, C.; Zhou, M.; Chen, Y. Atomically Precise Colloidal Metal Nanoclusters and Nanoparticles: Fundamentals and Opportunities. *Chem. Rev.* **2016**, *116*, 10346–10413.
4. Chakraborty, I.; Pradeep, T. Atomically Precise Clusters of Noble Metals: Emerging Link between Atoms and Nanoparticles. *Chem. Rev.* **2017**, *117*, 8208–8271.
5. Konishi, K. Phosphine-Coordinated Pure-Gold Clusters: Diverse Geometrical Structures and Unique Optical Properties/Responses. *Struct. Bond* **2014**, *161*, 49–86.
6. Lei, Z.; Wan, X.-K.; Yuan, S.-F.; Guan, Z.-J.; Wang, Q.-M. Alkynyl Approach toward the Protection of Metal Nanoclusters. *Acc. Chem. Res.* **2018**, *51*, 2465–2474.
7. Yao, Q.; Chen, T.; Yuan, X.; Xie, J. Toward Total Synthesis of Thiolate-Protected Metal Nanoclusters. *Acc. Chem. Res.* **2018**, *51*, 1338–1348.
8. Sakthivel, N. A.; Dass, A. Aromatic Thiolate-Protected Series of Gold Nanomolecules and a Contrary Structural Trend in Size Evolution. *Acc. Chem. Res.* **2018**, *51*, 1774–1783.
9. Bhattarai, B.; Zaker, Y.; Atnagulov, A.; Yoon, B.; Landman, U.; Bigioni, T. P. Chemistry and Structure of Silver Molecular Nanoparticles. *Acc. Chem. Res.* **2018**, *51*, 3104–3113.
10. Yan, J.; Teo, B. K.; Zheng, N. Surface Chemistry of Atomically Precise Coinage–Metal Nanoclusters: From Structural Control to Surface Reactivity and Catalysis. *Acc. Chem. Res.* **2018**, 51, 3084–3093.
11. Walter, M.; Akola, J.; Lopez-Acevedo, O.; Jadzinsky, P. D.; Calero, G.; Ackerson, C. J.; Whetten, R. L.; Grönbeck, H.; Häkkinen, H. A Unified View of Ligand-Protected Gold Clusters as Superatom Complexes. *Proc. Natl. Acad. Sci.* **2008**, *105*, 9157–9162.
12. Tang, Q.; Hu, G.; Fung, V.; Jiang, D. Insights into Interfaces, Stability, Electronic Properties, and Catalytic Activities of Atomically Precise Metal Nanoclusters from First Principles. *Acc. Chem. Res.* **2018**, *51*, 2793–2802.
13. Xu, W. W.; Zheng, X. C.; Gao, Y. Application of Electronic Counting Rules for Ligand-Protected Gold Nanoclusters. *Acc. Chem. Res.* **2018**, *51*, 2739–2747.
14. Aikens, C. M. Electronic and Geometric Structure, Optical Properties, and Excited State Behavior in Atomically Precise Thiolate-Stabilized Noble Metal Nanoclusters. *Acc. Chem. Res.* **2018**, *51*, 3065–6073.
15. Jadzinsky, P. D.; Calero, G.; Ackerson, C. J.; Bushnell, D. A.; Kornberg, R. D. Structure of a Thiol Monolayer-Protected Gold Nanoparticle at 1.1 Å Resolution. *Science* **2007**, *318*, 430–

433.

16. Heaven, M. W.; Dass, A.; White, P. S.; Holt, K. M.; Murray, R. M. Crystal Structure of the Gold Nanoparticle $[N(C_8H_{17})_4][Au_{25}(SCH_2CH_2Ph)_{18}]$ *J. Am. Chem. Soc.* **2008**, *130*, 3754–3755.
17. Zhu, M.; Aikens, C. M.; Hollander, F. J.; Schatz, G. C.; Jin, R. Correlating the Crystal Structure of A Thiol-Protected Au_{25} Cluster and Optical Properties. *J. Am. Chem. Soc.* **2008**, *130*, 5883–5885.
18. Yan, N.; Xia, N.; Liao, L.; Zhu, M.; Jin, F.; Jin, R.; Wu, Z. Unraveling the Long-Pursued Au_{144} Structure by x-Ray Crystallography. *Sci. Adv.* **2018**, *4*, eaat7259.
19. Jin, R. Atomically Precise Metal Nanoclusters: Stable Sizes and Optical Properties. *Nanoscale* **2015**, *7*, 1549–1565.
20. Negishi, Y.; Nakazaki, T.; Malola, S.; Takano, S.; Niihori, Y.; Kurashige, W.; Yamazoe, S.; Tsukuda, T.; Häkkinen, H. A Critical Size for Emergence of Nonbulk Electronic and Geometric Structures in Dodecanethiolate-Protected Au Clusters. *J. Am. Chem. Soc.* **2015**, *137*, 1206–1212.
21. Kwak, K.; Lee, D. Electrochemistry of Atomically Precise Metal Nanoclusters. *Acc. Chem. Res.* **2019**, *52*, 12–22.
22. Yau, S. H.; Varnavski, O.; Goodson III, T. An Ultrafast Look at Au Nanoclusters. *Acc. Chem. Res.* **2013**, *46*, 1506–1516.
23. Yi, C.; Zheng, H.; Herbert, P. J.; Chen, Y.; Jin, R. Knappenberger, Jr. Ligand- and Solvent-Dependent Electronic Relaxation Dynamics of $Au_{25}(SR)_{18}^-$ Monolayer-Protected Clusters. *J. Phys. Chem. C* **2017**, *121*, 24894–24902.
24. Kwak, K.; Thanthirige, V. D.; Pyo, K.; Lee, D.; Ramakrishna, G. Energy Gap Law for Exciton Dynamics in Gold Cluster Molecules. *J. Phys. Chem. Lett.* **2017**, *8*, 4898–4905
25. Negishi, Y.; Nobusada, K.; Tsukuda, T. Glutathione-Protected Gold Clusters Revisited: Bridging the Gap between Gold(I)-Thiolate Complexes and Thiolate-Protected Gold Nanocrystals. *J. Am. Chem. Soc.* **2005**, *127*, 5261–5270.
26. Kang, X.; Chong, H.; Zhu, M. $Au_{25}(SR)_{18}$: the Captain of the Great Nanocluster Ship. *Nanoscale*, **2018**, *10*, 10758.
27. Joshi, C. P.; Bootharaju, M. S.; Alhilaly, M. J.; Bakr, O. M. $[Ag_{25}(SR)_{18}]^-$: The "Golden" Silver Nanoparticle. *J. Am. Chem. Soc.* **2015**, *137*, 11578–11581.
28. Schacht, J.; Gaston, N. From the Superatom Model to a Diverse Array of Superelements: A Systematic Study of Dopant Influence on the Electronic Structure of Thiolate-Protected Gold Clusters. *ChemPhysChem* **2016**, *17*, 3237–3244.
29. Yu, P.; Wen, X.; Toh, Y.; Huang, J.; Tang, J. Metallophilic Bond-Induced Quenching of Delayed Fluorescence in Au_{25}@BSA Nanoclusters. *Part. Part. Syst. Charact.* **2013**, *30*, 467–

472.

30. Katla, S. K.; Zhang, J.; Castro, E.; Bernal, R. A.; Li, X. Atomically Precise $Au_{25}(SG)_{18}$ Nanoclusters: Rapid Single-Step Synthesis and Application in Photothermal Therapy. *ACS Appl. Mater. Interfaces* **2018**, *10*, 75–82.
31. Yu, C.; Li, G.; Kumar, S.; Kawasaki, H.; Jin, R. Stable $Au_{25}(SR)_{18}/TiO_2$ Composite Nanostructure with Enhanced Visible Light Photocatalytic Activity. *J. Phys. Chem. C* **2013**, *4*, 2847–2852.
32. Agrachev, M.; Ruzzi, M.; Venzo, A.; Maran, F. Nuclear and Electron Magnetic Resonance Spectroscopies of Atomically Precise Gold Nanoclusters. *Acc. Chem. Res.* **2019**, *52*, 44–52.
33. Ohta, T., Shibuta, M., Tsunoyama, H., Negishi, Y., Eguchi, T., Nakajima, A. Size and Structure Dependence of Electronic States in Thiolate-Protected Gold Nanoclusters of $Au_{25}(SR)_{18}$, $Au_{38}(SR)_{24}$, and $Au_{144}(SR)_{60}$. *J. Phys. Chem. C* **2013,** *117*, 3674–3679.
34. Jiang, D.; Kühn, M.; Tang, Q.; Weigend, F. Superatomic Orbitals under Spin-Orbit Coupling. *J. Phys. Chem. Lett.* **2014**, *5*, 3286–3289.
35. Tofanelli, M. A.; Salorinne, K.; Ni, T. W.; Malola, S.; Newell, B.; Phillips, B.; Häkkinen, H.; Ackerson, C. Jahn–Teller Effects in $Au_{25}(SR)_{18}$. *Chem. Sci.* **2016**, *7*, 1882–1890.
36. Hamouda, R.; Bellina, B.; Bertorelle, F.; Compagnon, I.; Antoine, R.; Broyer, M.; Rayane, D.; Dugourd, P. Electron Emission of Gas-Phase $[Au_{25}(SG)_{18}\text{-}6H]^{7-}$ Gold Cluster and Its Action Spectroscopy. *J. Phys. Chem. Lett.* **2010**, *1*, 3189–3194.
37. Akola, J.; Walter, M.; Whetten, R. L.; Häkkinen, H.; Grönbeck, H. On the Structure of Thiolate-Protected Au_{25}. *J. Am. Chem. Soc.* **2008**, *130*, 3756–3757.
38. Kacprzak, K. A.; Lehtovaara, L.; Akola, J.; Lopez-Acevedo, O.; Häkkinen, H. A Density Functional Investigation of Thiolate-Protected Bimetal $PdAu_{24}(SR)_{18}^{z}$ Clusters: Doping the Superatom Complex. *Phys. Chem. Chem. Phys.* **2009**, *11*, 7123–7129.
39. Jung, J.; Kang, S.; Han Y.-K. Ligand Effects on the Stability of Thiol-Stabilized Gold Nanoclusters: $Au_{25}(SR)_{18}^{-}$, $Au_{38}(SR)_{24}$, and $Au_{102}(SR)_{44}$. *Nanoscale* **2012**, *4*, 4206–4210.
40. Taylor, K. J.; Pettiette-Hall, C. L.; Cheshnovsky, O.; Smalley, R. E. Ultraviolet Photoelectron Spectra of Coinage Metal Clusters. *J. Chem. Phys.* **1993**, *65*, 611–676.
41. Ning, C.-G.; Xiong, X.-G.; Wang, Y.-L.; Li, J.; Wang, L.-S. Probing the Electronic Structure and Chemical Bonding of the "Staple" Motifs of Thiolate Gold Nanoparticles: $Au(SCH_3)_2^{-}$ and $Au_2(SCH_3)_3^{-}$. *Phys. Chem. Chem. Phys.* **2012**, *14*, 9323–9329.
42. Black, D. M.; Crittenden, C. M.; Brodbelt, J. S.; Whetten, R. L. Ultraviolet Photodissociation of Selected Gold Clusters: Ultraefficient Unstapling and Ligand Stripping of $Au_{25}(pMBA)_{18}$ and $Au_{36}(pMBA)_{24}$. *J. Phys. Chem. Lett.* **2017**, *8*, 1283–1289.
43. Weidele, H.; Kreisle, D.; Recknagel, E.; Icking-Konert, G. S.; Handschuh, H.; Ganteför, G.; Eberhartdt. W. Thermionic Emission from Small Clusters: Direct Observation of the Kinetic

Energy Distribution of the Electrons. *Chem. Phys. Lett.* **1995**, *237*, 425–431.

44. Ganteför, G.; Eberhardt, W.; Weidele, H.; Kreisle, D.; Recknagel, E. Energy Dissipation in Small Clusters: Direct Photoemission, Dissociation, and Thermionic Emission. *Phys. Rev. Lett.* **1996**, *77*, 4524–4527.
45. Mooney, C. R. S.; Parkes, M. A.; Iskra, A.; Fielding, H. H. Controlling Radical Formation in the Photoactive Yellow Protein Chromophore. *Angew. Chem. Int. Ed.* **2015**, *54*, 5646–5649.
46. Liu, C.; Lin, S.; Pei, Y.; Zeng, X. C. Semiring Chemistry of $Au_{25}(SR)_{18}$: Fragmentation Pathway and Catalytic Active Site. *J. Am. Chem. Soc.* **2013**, *135*, 18067–18079.

Chapter 3.

Ion mobility mass spectrometry of $[PdAu_8(PPh_3)_8]^{2+}$ and $[Au_9(PPh_3)_8]^{3+}$

Hirata, K.; Chakraborty, P.; Nag, A.; Takano, S.; Koyasu, K.;

Pradeep, T.; Tsukuda, T.

J. Phys. Chem. C **2018**, *122*, 23123–23128.

3.1 Introduction

As mentioned in Chapter 1, ligand-protected metal clusters have extended the scope of materials science owing to their novel properties.[1–9] The key descriptors through which we can tune the properties and functions of protected metal clusters are the number (cluster size) and composition of metal atoms at the core. There are many examples illustrating how the optical, catalytic, and magnetic properties of protected metal clusters are affected by their size and composition.

However, the properties and functions of such clusters are not only decided by size and composition, but also by the geometric structure. Especially, the atomic packing of the metallic core is an important parameter because protected metal clusters can take a variety of structural isomers[10,11] and the electronic structures are strongly coupled with the core structures. For example, optical spectra of structural isomers $Au_{28}(SPh^tBu)_{20}$ and $Au_{28}(Sc\text{-}C_6H_{11})_{20}$ exhibit different profiles reflecting the difference in the core structures.[10] Another example is that the optical absorption spectrum is strongly dependent on temperature[12] due to thermal fluctuation of the metallic core.[13] The structure of the ligand layer is also an important parameter determining the physicochemical properties including chirality,[14,15] nonlinear optical activity[16] and electron transfer reactions.[17] While the monolayer of alkanethiolates on an Au cluster exhibits a dispersed state, that in the solid state forms a bundle-like structure.[18] The electron transfer reaction for an alkanethiolate ($C_nH_{2n+1}S$)-protected Au_{25} cluster is independent of n in the range of 12–18 due to the formation of a bundle-like structure.[17]

As mentioned in Chapter 1, several unique techniques have been recently used for the structural characterization of protected metal clusters isolated in vacuum. The methods include ion mobility mass spectrometry (IMMS),[19–22] collision-induced

dissociation mass spectrometry (CIDMS),[23–25] photodissociation mass spectrometry (PDMS)[26] and photoelectron spectroscopy (PES).[27] These methods provide essential information on the stability and structures without any influence from the dispersion media. For example, Laskin and Johnson reported IMMS of $[Au_8(PPh_3)_{7-x}(PPh_2Me)_x]^{2+}$ as a function of x and found that arrival times decrease abruptly from x = 3 to 4.[22] This behavior was ascribed to the formation of a closely packed arrangement of the phosphine ligands due to dispersion interactions. However, several interesting questions remained unaddressed using IMMS: (1) Does the CCS value determined by IMMS quantitatively reproduce those for the structures determined by X-ray crystallography? (2) Does the CCS value reflect the structure of the protected metal clusters in the dispersion? (3) Can we probe collision-induced isomerization by IMMS?

To address the above issues, we conducted IMMS measurements on $[PdAu_8(PPh_3)]^{2+}$ and $[Au_9(PPh_3)_8]^{3+}$, the structures of which have been determined by single-crystal X-ray analysis (Figure 3.1).[28–32] $[PdAu_8(PPh_3)_8]^{2+}$ takes a crown motif (Figure 3.1a), while

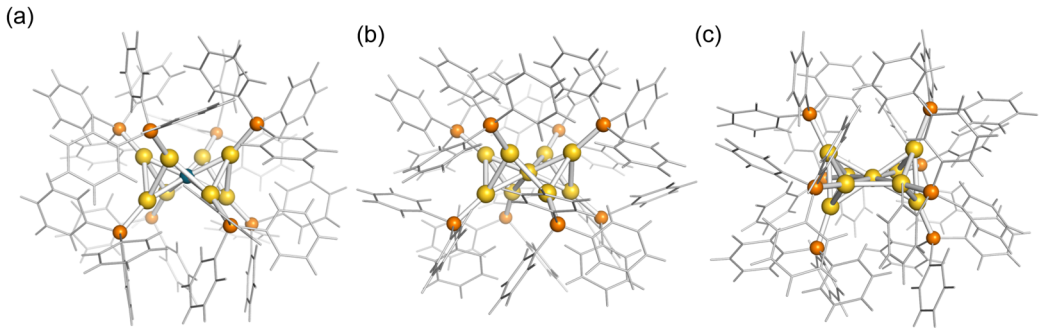

Figure 3.1 Crystal structures of (a) $[PdAu_8(PPh_3)_8]^{2+}$ with a crown motif and $[Au_9(PPh_3)_8]^{3+}$ with (b) crown and (c) butterfly motifs. Orange, blue, and purple colors indicate Au, Pd, and P atoms, respectively. Ph group is shown by wireframe.

$[Au_9(PPh_3)_8]^{3+}$ can take two isomeric forms in the crystal phase, a crown (Cr) or a butterfly (Bt) motif, depending on the size of the counter anions (Figures 3.1b and

c).[28,29,32] The single-crystal structures shown in Figures 3.1a–c are hereafter referred to as **$PdAu_8$(Cr)**, **Au_9(Cr)**, and **Au_9(Bt)**, respectively. The absence of a butterfly motif in $[PdAu_8(PPh_3)_8]^{2+}$ is ascribed to suppression of the core isomerization due to stiffening of the intracluster bonds by Pd doping.[33] Their metallic cores $[Au_9]^{3+}$ and $[PdAu_8]^{2+}$ can be viewed as oblate-shaped superatoms with an electron configuration of $(1S)^2(1P)^4$.[31,34] Close inspection of **$PdAu_8$(Cr)** and **Au_9(Cr)** reveals that the structures of the ligand layers are different although their cores have crown motifs; CH–π and π–π interactions between the phenyl rings of adjacent PPh_3 ligands, respectively, play a role in determining the structures of the ligand layers (Figure 3.2). $[PdAu_8(PPh_3)]^{2+}$ and $[Au_9(PPh_3)_8]^{3+}$ are ideal clusters to probe core isomerization and ligand rearrangement. We determined by IMMS the CCS values of electrosprayed $[PdAu_8(PPh_3)_8]^{2+}$ and $[Au_9(PPh_3)_8]^{3+}$ and compared them with those of the structures determined by X-ray crystallography. The results showed that the disordered ligand layers of $[PdAu_8(PPh_3)_8]^{2+}$ and $[Au_9(PPh_3)_8]^{3+}$ in dispersion are retained during desolvation by electrospray ionization (ESI), but can be converted to more compact structures found in single crystals via collisional excitation and cooling.

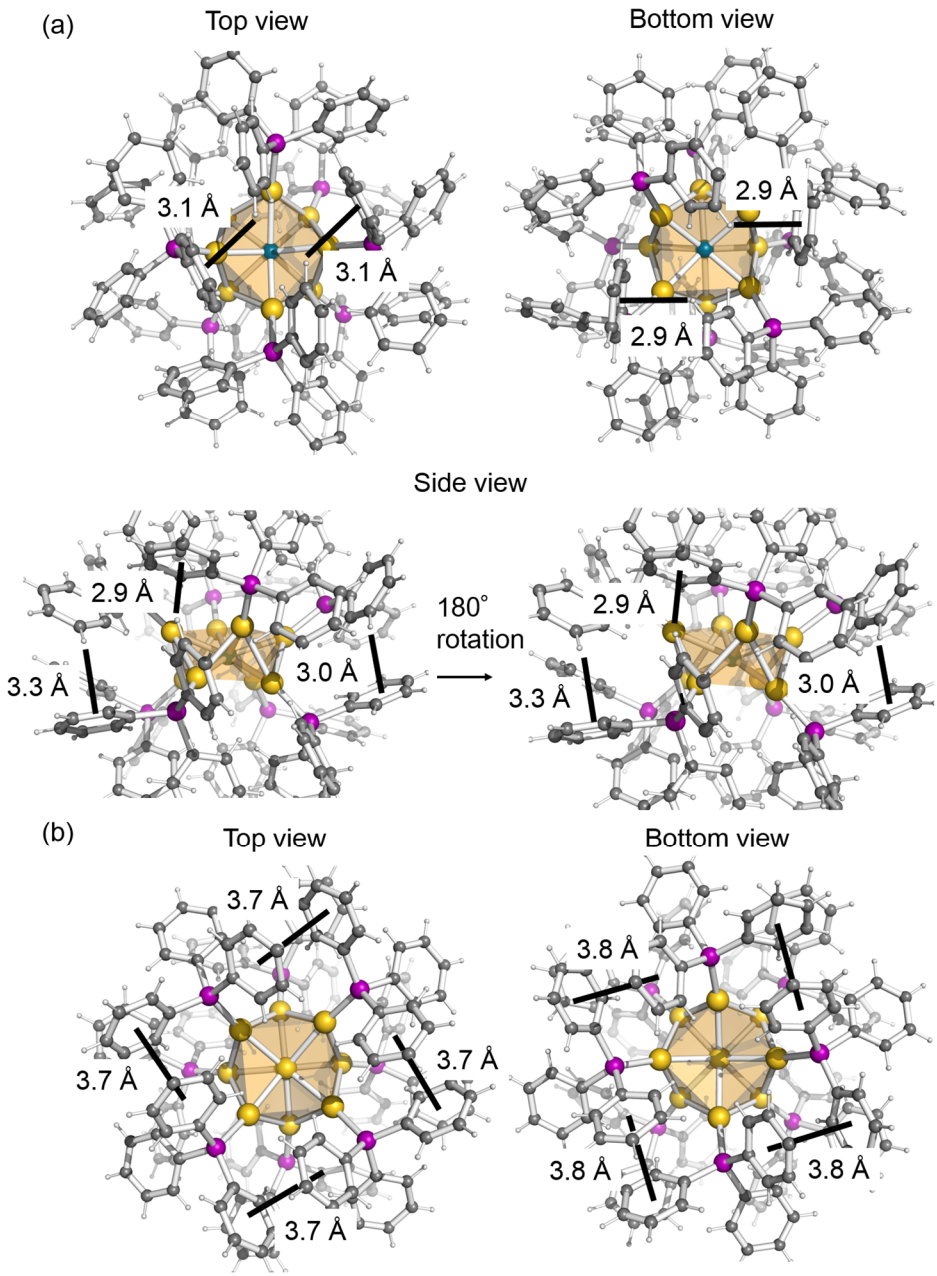

Figure 3.2 Ligand packing in the crown-shaped crystals of (a) $[PdAu_8(PPh_3)_8](NO_3)_2$ and (b) $[Au_9(PPh_3)_8](PW_{12}O_{40})$. Orange, blue, and purple colors indicate Au, Pd, and P atoms, respectively.

3.2 Methods

3.2.1 Experimental

3.2.1.1 Synthesis

$[Au_9(PPh_3)_8](NO_3)_3$ was chemically synthesized by a method previously reported.[33] First, ethanol solution (13 mL) of $NaBH_4$ (9.4 mg, 0.25 mmol) was added to another ethanol solution (13 mL) of $Au(NO_3)(PPh_3)$ (521 mg, 1.0 mmol). The mixture was filtrated after stirring for 15 min at room temperature and the filtrate was evaporated. The residue was poured into tetrahydrofurane (THF) (35 mL) and stood still overnight. The precipitate was collected by filtration and washed with THF and hexane. The green solid (95 mg) was obtained by evaporating the residual solvent. $[PdAu_8(PPh_3)_8](NO_3)_2$ was synthesized by a similar method.[33] Dichloromethane solution (20 mL) of $Pd(PPh_3)_4$ (115 mg, 0.10 mmol) was quickly added to that (20 mL) of $Au(NO_3)(PPh_3)$ (421 mg, 0.81 mmol). After stirring for 1 min, ethanol solution (15 mL) of $NaBH_4$ (20 mg, 0.53 mmol) was quickly added into the mixture. The mixture was evaporated after stirring for 1 min. The residue was poured into methanol (10 mL). The precipitate was filtrated and mixed with acetone (5 mL). The precipitate was filtrated and poured into methanol (50 mL). Diethylether (70 mL) was slowly added into the solution to precipitate $[PdAu_8(PPh_3)_8](NO_3)_2$. The brownish solid (193 mg) was obtained by filtration followed by washing with diethylether and hexane. Both samples were characterized by UV-vis absorption spectroscopy.

3.2.1.2 Overview of the experimental setup

Mass spectra and arrival time distributions (ATDs) were measured using an ion mobility mass spectrometer (Synapt G2-Si, Waters Corp., Manchester, U.K.) installed at

IIT Madras (Figure 3.3).[21,35,36] The apparatus consists of an ESI source, a traveling wave ion guide (TWIG), a quadrupole mass filter, a trapping TWIG (not shown in Figure 3.3), a Helium cell, a traveling wave ion mobility (TWIM) cell and a time-of-flight mass spectrometer (TOFMS) equipped with a reflectron. $[PdAu_8(PPh_3)_8](NO_3)_2$ or $[Au_9(PPh_3)_8](NO_3)_3$ dispersed in methanol was introduced into the mass spectrometer via the ESI source. Neutral species were eliminated by the TWIG. The ions of interest guided by the TWIG were mass-selected by the quadrupole mass filter. The mass-selected cationic clusters were continuously stored in the trapping TWIG. The ions thus stored were injected periodically into the He and TWIM cells[35] by applying a pulsed voltage to the gate electrode. The pressures in the cells were raised up to 100–300 Pa by flowing He and N_2 gases. The flow rate of the He and N_2 gases (F_{He} and F_{N2}) was controlled in the range of 0–150 and 45–55 mL min^{-1}, respectively. The pulsed ion beam enters the He cell and the kinetic energy of the ions was decreased by collisions with buffer He gas. The ions in the TWIM cell were slowed by the collisions with buffer N_2 gas and were propelled by the electric filed applied in the TWIM cell. The voltage was periodically applied to the electrodes in the TWIM cell to generate a traveling wave with a triangular voltage profile. The ions were ejected from the cell according to the mobility (or collision frequency with buffer gas) of ions.[35] The ions thus separated based on the mobility were orthogonally extracted by a pulsed electric field between the acceleration grids and were detected by the TOFMS. The ion intensities of the parent ions were monitored by the TOFMS with varying a time between injection to the He cell and pulsed extraction at the TOFMS.

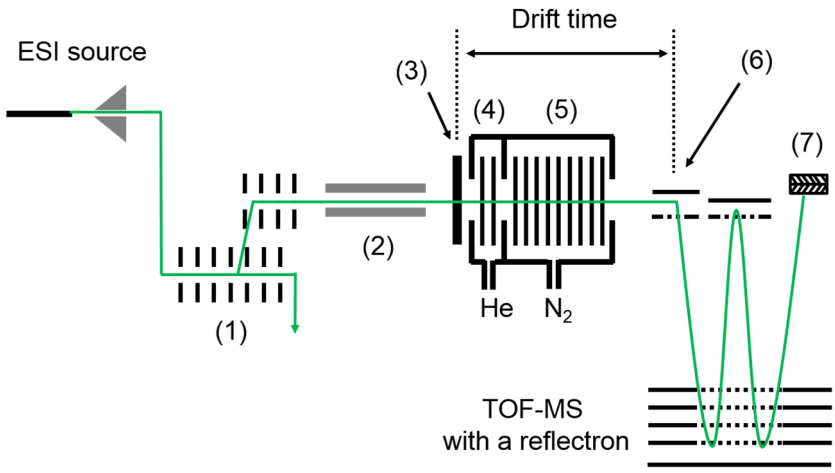

Figure 3.3 Schematic illustration of the experimental apparatus. (1) Traveling wave ion guides (TWIG), (2) a quadrupole mass filter, (3) a gate electrode, (4) a He cell, (5) a traveling wave ion mobility (TWIM) cell, (6) acceleration grids, and (7) an ion detector. Green line indicates ion trajectory.

3.2.1.3 Ion mobility mass spectrometry

The ATD was obtained by plotting the intensities of $[PdAu_8(PPh_3)_8]^{2+}$ or $[Au_9(PPh_3)_8]^{3+}$ as a function of the time difference between the ion injection into the He cell and ion extraction at the TOFMS. Thus, the arrival time giving the peak of ATD (AT_{max}) is expressed by:

$$AT_{max} = T_{cell} + T_{drift} = \frac{\sqrt{\mu}}{z} A\Omega_{exp}{}^{B} + c\sqrt{\frac{m}{z}} \qquad (3.1)$$

where T_{cell} and T_{drift} represent the drift time spent in the cell and that spent from the exit of the cell to the acceleration region of the TOFMS.[37–39] The terms m, z, μ, and Ω_{exp} are the ion mass, the charge, the reduced mass of the clusters and the buffer gas, and the CCS, respectively. The constants A and B were calibrated with the experimental data on myoglobin collected at F_{He} and F_{N2} of 43.2 and 55 mL min^{-1}, respectively, and at room temperature.[40] Acetonitrile/water mixed solution (1:1, v/v) containing myoglobin with 0.1% of formic acid added was electrosprayed. The constant c was obtained from

commercially available software.[39] Key experimental parameters are listed in the Table 3.1.

Table 3.1 Apparatus parameters.

	Calibration	Figure 3.4	Figure 3.5	Figure 3.6
Capillary bias (kV)	3.5	3.0	3.5	2.0
Source temp. (°C)	100	100	100	100
Sampling core (V)	40	20	0	0
Source offset (V)	60	20	0	0
Desolvation temp. (°C)	150	150	150	150
Cone gas flow (L hr^{-1})	0	0	0	0
Desolvation gas flow (L hr−^{1})	400	400	400	400
Nebulizer gas (bar)	2.5	2.5	2.5	2.5
Trap gas flow (mL min^{-1})	0	0	0	0
Helium cell gas flow (mL min^{-1})	43.2	0–150	35–80	43.2
IMS gas flow (mL min^{-1})	55	45	55	47.3
Sample infusion flow rate (μL min^{-1})	10	10	10	20
Trap DC entrance (V)	0	0	0	0
Trap DC bias (V)	25.6	27.2	25.6	24.1
Trap DC exit (V)	0	3.0	0	0
Transfer voltage (V)	0	0	0	2
IMS wave velocity (m s^{-1})	650	700	650	658

IMS wave height (m s^{-1})	40	40	25	38.2

3.2.2 Theoretical calculation

The CCS values of **$PdAu_8$(Cr)**, **Au_9(Cr)**, and **Au_9(Bt)** were calculated by three methods: the diffuse-hard-sphere scattering (DHSS),[41] projection approximation (PA)[41] and exact hard-sphere scattering (EHSS) methods.[43] The DHSS method assumes that the cluster consists of hard-sphere atoms. According to Ref. 41, we assumed that 91% of the collisions between the buffer gas (N_2) and the cluster are inelastic and diffusive and the remaining 9% of the collisions are elastic and specular. The atomic radii of Au, Pd, P, C, and H atoms were set to 1.66, 2.0, 1.8, 1.7, and 1.1 Å, respectively. An N_2 molecule was regarded as a sphere with a radius of 1.5 Å. The clusters were rotated three times in a surrounding environment of 30000 N_2 molecules during the simulation for DHSS. The re-emission velocity of gas molecules after collision was assumed to have a Maxwell distribution. In the PA method, the CCS value was determined by projecting a three-dimensional ion geometry onto a two-dimensional plane and averaging all the possible geometries assuming a hard-sphere model. The clusters were rotated 100 times in a surrounding environment of 30000 N_2 molecules during the simulation. In the EHSS method, all the collision events with N_2 gas were assumed to be completely elastic. The temperature and N_2 pressure used in these calculations were 300 K and 290 Pa, respectively. IMoS software[44] was used for calculations.

3.3 Results and discussion

3.3.1 Pressure-dependent arrival time distributions

The ATDs of $[PdAu_8(PPh_3)_8]^{2+}$ are shown in Figure 3.4 as a function of F_{He}. The

ATDs exhibit a single peak β when F_{He} is higher than 120 mL min^{-1} (Figures 3.4a and 3.4b). When F_{He} is reduced to 80 mL min^{-1}, a new peak α appears as a hump at the shorter arrival time side of peak β (Figure 3.4c). Relative intensity of peak α with respect to peak β increases with the decrease in F_{He} (Figures 3.4d–f) and peak α dominates the ATD when F_{He} is reduced to 0 mL min^{-1} (Figure 3.4g). The decrease in F_{He} leads to a decrease of collision frequency of the target cluster and to an increase in the mean free path. As a result, the ions in the He cell gain more kinetic energy from the traveling electric field, collide with the N_2 gas with a higher collision energy and exit the cell in shorter time under low pressure. Therefore, the transformation from peak β to peak α in Figure 3.4 indicates that an isomer for peak β (**$PdAu_8$(B)**) is "converted" to a more compact isomer for peak α (**$PdAu_8$(A)**) by collisional heating. The gradual decrease in the total ion intensities is due to the CID of $[PdAu_8(PPh_3)_8]^{2+}$.

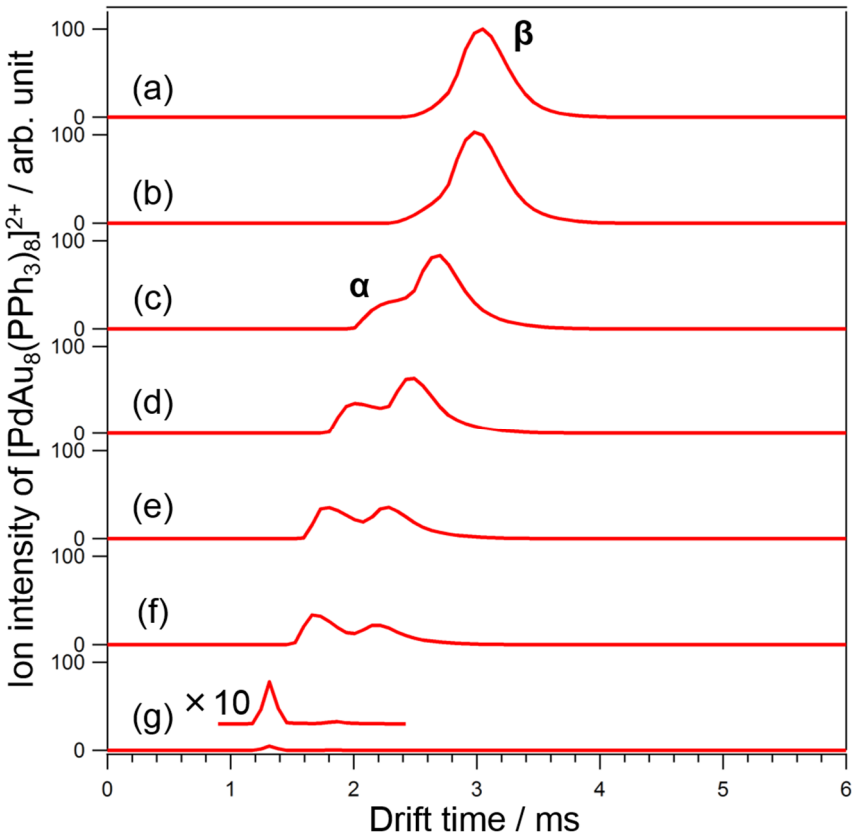

Figure 3.4 Arrival time distributions of $[PdAu_8(PPh_3)_8]^{2+}$ at F_{N2} = 45 and F_{He} = (a) 150, (b) 120, (c) 80, (d) 60, (e) 43, (f) 35, and (g) 0 mL min^{-1}.

A similar behavior was observed in the ATD of $[Au_9(PPh_3)_8]^{3+}$ recorded in the range of F_{He} = 35–80 mL min^{-1} (Figure 3.5). This figure clearly shows that the relative abundance of **Au_9(C)** giving peak γ with respect to **Au_9(D)** giving peak δ increases with decrease of F_{He}. This result indicates that **Au_9(D)** is converted into the more compact **Au_9(C)** upon collisional excitation and cooling. The more rapid decrease in the intensity of $[Au_9(PPh_3)_8]^{3+}$ than $[PdAu_8(PPh_3)_8]^{2+}$ at lower F_{He} is associated with the fact that the former is more easily dissociated into fragment ions.

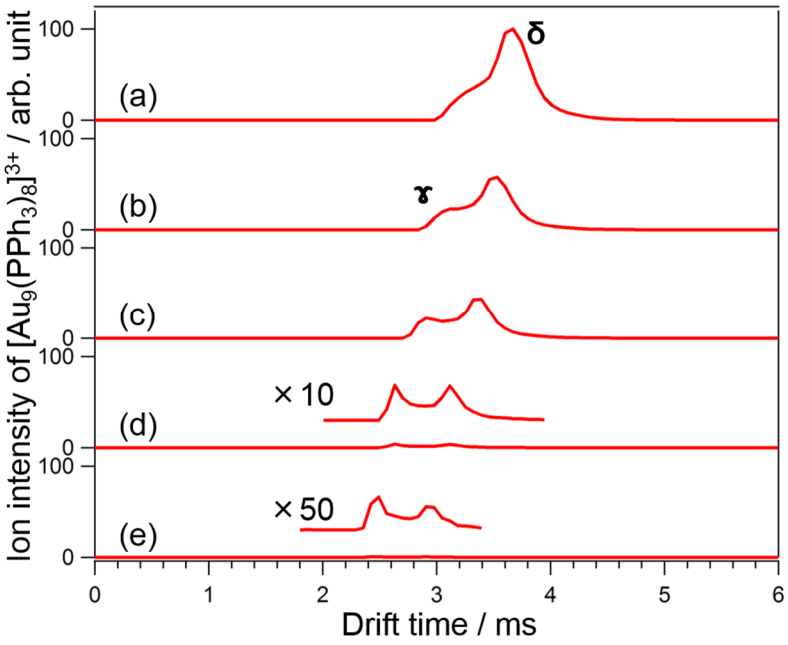

Figure 3.5 Arrival time distributions of $[Au_9(PPh_3)_8]^{3+}$ at F_{N2} = 55 and F_{He} = (a) 80, (b) 70, (c) 60, (d) 45, and (e) 35 mL min^{-1}.

3.3.2 Experimental and theoretical collision cross section values

To help the assignment of structural isomers found in section 3.1, we compared the CCS values experimentally determined (Ω_{exp}) and those calculated for the single-crystal structures in Figure 3.1 (Ω_{calcn}). The ATDs of $[PdAu_8(PPh_3)_8]^{2+}$ and $[Au_9(PPh_3)_8]^{3+}$ were dominated by peaks β and δ assigned to **$PdAu_8$(B)** and **Au_9(D)**, respectively, at F_{He} = 43.2 and F_{N2} = 55 mL min^{-1} employed for calibration. The Ω_{exp} values for **$PdAu_8$(B)** and **Au_9(D)** were determined to be 422 and 442 $Å^2$ using Eq. 3.1. (Table 3.2). Peak α for **$PdAu_8$(A)** and peak γ for **Au_9(C)** emerged with slight alteration of F_{N2}, wave velocity, and wave height as shown in Figure 3.6 (parameters are shown in the Table 3.1). The Ω_{exp} values for **$PdAu_8$(A)** and **Au_9(C)** were determined to be 404 and 402 $Å^2$, respectively, using that for **$PdAu_8$(B)** as a reference. The Ω_{exp} values for all the isomers were

reproduced within the statistical error of ~1%.

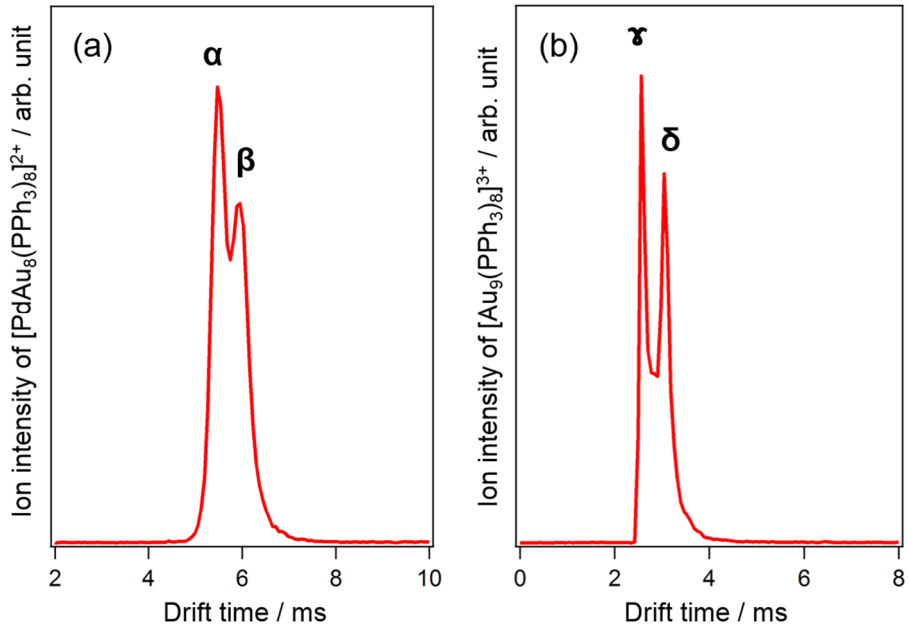

Figure 3.6 Arrival time distributions of (a) $[PdAu_8(PPh_3)_8]^{2+}$ and (b) $[Au_9(PPh_3)_8]^{3+}$ recorded at F_{He} = 43.2 and F_{N2} = 47.2 mL min^{-1}.

Table 3.2 The experimental CCS values

Isomer	Peak	Ω_{exp} (Å^2)[a]
$PdAu_8$(A)	α	404
$PdAu_8$(B)	β	422
Au_9(C)	γ	402
Au_9(D)	δ	442

[a]CCS value experimentally determined.

The Ω_{calcn} values obtained by the DHSS, PA and EHSS methods for **$PdAu_8$(Cr)**, **Au_9(Cr)** and **Au_9(Bt)** are listed in Table 3.3. The Ω_{calcn} values are strongly dependent on the calculation methods. Especially, the DHSS method overestimates the Ω_{exp} values significantly, although it was reported that DHSS reproduced the Ω_{exp} values determined using diatomic and polarizable molecules such as N_2 as buffer gas better than other methods such as PA and EHSS.[41] This result suggests that N_2 molecules collide with the

clusters in an elastic manner. In addition, there was no appreciable difference in the Ω_{calcn} values for the two isomers of **Au_9(Cr)** and **Au_9(Bt)**, indicating that IMMS cannot differentiate isomers having different core structures in the present case.

Table 3.3 Theoretical CCS values

Structure	Ω_{calcn} (Å^2)[a]		
	DHSS	PA	EHSS
$PdAu_8$(Cr)	514	367	420
Au_9(Cr)	509	365	413
Au_9(Bt)	514	366	416

[a]CCS value theoretically calculated.

3.3.3 Collision-induced isomerization

Significant discrepancies between Ω_{exp} and Ω_{calcn} do not allow us to make a straightforward assignment of the isomers in Table 3.2. In **$PdAu_8$(Cr)**, the PPh_3 layer forms a densely packed structure around the core due to CH–π interactions between the phenyl rings of adjacent PPh_3 ligands. Because no other isomer having a more compact packing than **$PdAu_8$(Cr)** is available, we assign **$PdAu_8$(A)** to **$PdAu_8$(Cr)**. Since no other isomer with a different core structure is known for $[PdAu_8(PPh_3)_8]^{2+}$, it is reasonable to assign **$PdAu_8$(B)** to a less stable isomer having poorly packed ligand structures compared to **$PdAu_8$(Cr)**. This assignment leads us to conclude that the structure of $[PdAu_8(PPh_3)_8]^{2+}$ introduced into vacuum via the ESI source is different from **$PdAu_8$(Cr)** in terms of the ligand packing. Probably, the structure of the ligand layer of **$PdAu_8$(B)** introduced in the gas phase via the ESI source is similar to that in the dispersion, which is determined by the balance between the ligand-to-ligand and ligand-to-solvent interactions. During the desolvation process in the ESI source, the disordered packings of the ligand layer may be frozen at various metastable states. Upon the collisional activation

and subsequent collisional cooling, the ligand layer of **$PdAu_8$(B)** is annealed into the most stable, densely packed structure with the maximal ligand-to-ligand interaction similar to that in the crystal.

Given that the core of $[Au_9(PPh_3)]^{3+}$ takes the crown motif in dispersion, it is reasonable to assign the final species **Au_9(C)** to **Au_9(Cr)** found in the crystalline phase. **Au_9(D)** was assigned to an isomer having poorly packed ligand structures. Thus, the isomerization from **Au_9(D)** to **Au_9(C)** in Figure 3.5 can be explained by a collision-induced crystallization of the ligand layer. However, we cannot exclude the possibility that core isomerization from the crown to the butterfly also occurred because their Ω_{calcn} values are very close (Table 3.3). Table 1 shows that the Ω_{calcn} value of **Au_9(D)** (442 $Å^2$) is much larger than that of **$PdAu_8$(B)** (422 $Å^2$). This may suggest that **Au_9(D)** takes a more expanded core than **Au_9(Cr)** reflecting the softer Au–Au bonds than Pd–Au bonds in **$PdAu_8$(Cr)**.[33]

3.4 Conclusion

The CCS values of $[PdAu_8(PPh_3)_8]^{2+}$ and $[Au_9(PPh_3)_8]^{3+}$, electrosprayed into the gas phase, were determined by IMMS and they were found to be 422 and 442 $Å^2$, respectively. With the reduction of the flow rates of He into the cell, $[PdAu_8(PPh_3)_8]^{2+}$ and $[Au_9(PPh_3)_8]^{3+}$ underwent collision-induced isomerization to smaller species with the CCS values of 404 and 402 $Å^2$, respectively. However, the CCS values theoretically calculated for their single-crystal structures were in the range of 360–520 $Å^2$ depending on the calculation methods. We interpret the experimental observations to conversion of the clusters with disordered ligand layers in the solution into their single-crystal structures with packed ligand layers. The present study illustrates that IM MS will be useful for

structural characterization in ligand-protected metal clusters in solutions and for understanding their isomers in the gas phase.

References

1. Häkkinen, H. Atomic and Electronic Structure of Gold Clusters: Understanding Flake, Cages and Superatoms from Simple Concepts. *Chem. Soc. Rev.* **2008**, *37*, 1847–1859.
2. Jin, R. Quantum Sized, Thiolate-protected Gold Nanoclusters. *Nanoscale* **2010**, *2*, 343–362.
3. Maity, P.; Xie, S.; Yamauchi, M.; Tsukuda, T. Stabilized Gold Clusters: From Isolation Toward Controlled Synthesis. *Nanoscale* **2012**, *4*, 4027–4038.
4. Konishi, K. Phosphine-Coordinated Pure-Gold Clusters: Diverse Geometrical Structures and Unique Optical Properties/Responses. *Struct. Bond* **2014**, *161*, 49–86.
5. Tsukuda, T.; Häkkinen, H. Protected Metal Clusters: From Fundamentals to Applications, 1st ed.; Elsevier, B. V.: Amsterdam, The Netherlands, 2015.
6. Fernando, A.; Weerawardene, K. L. D.; Karimova, N.; Aikens, C. M. Quantum Mechanical Studies of Large Metal, Metal Oxide, and Metal Chalcogenide Nanoparticles and Clusters. *Chem. Rev*. **2015**, *115*, 6112–6216.
7. Jin, R.; Zhen, C.; Zhou, M.; Chen, X. Atomically Precise Colloidal Metal Nanoclusters and Nanoparticles: Fundamentals and Opportunities. *Chem. Rev*. **2016**, *116*, 10346–10413.
8. Kurashige, W.; Niihori, Y.; Sharma, S.; Negishi, Y. Precise Synthesis, Functionalization and Application of Thiolate-Protected Gold Clusters. *Coord. Chem. Rev*. **2016**, *320–321*, 238–250.
9. Chakraborty, I.; Pradeep, T. Atomically Precise Clusters of Noble Metals: Emerging Link between Atoms and Nanoparticles. *Chem. Rev*. **2017**, *117*, 8208–8271.
10. Chen, Y.; Liu, C.; Tang, Q.; Zeng, C.; Higaki, T.; Das, A.; Jiang, D.; Rosi, L. N.; Jin, R. Isomerism in $Au_{28}(SR)_{20}$ Nanocluster and Stable Structures. *J. Am. Chem. Soc.* **2016**, *138*, 1482–1485.
11. Jensen, K. M. Ø.; Juhas, P.; Tofanelli, M. A.; Heinecke, C. L.; Vaughan, G.; Ackerson, C. J.; Billinge, S. J. L. Polymorphism in Magic-Sized $Au_{144}(SR)_{60}$ Clusters. *Nat. Commun.* **2016**, *7*, 11859.
12. Devadas, M. S.; Bairu, S.; Qian, H.; Sinn, E.; Jin, R.; Ramakrishna, G. Temperature-Dependent Optical Absorption Properties of Monolayer-Protected Au_{25} and Au_{38} Clusters. *J. Phys. Chem. Lett.* **2011**, *2*, 2752–2758.
13. Yamazoe, S.; Takano, S.; Kurashige, W.; Yokoyama, T.; Nitta, K.; Negishi, Y.; Tsukuda, T. Hierarchy of bond stiffness within icosahedral-based gold clusters protected by thiolates. *Nat. Commun.* **2016**, *5*, 10414.
14. Knoppe, S.; Bürgi, T. Chirality in Thiolate-Protected Gold Clusters. *Acc. Chem. Res*. **2014**, *47*, 1318–1326.
15. Takano, S.; Tsukuda, T. Amplification of Optical Activity of Gold Clusters by the Proximity of BINAP. *J. Phys. Chem. Lett*. **2016**, *7*, 4509–4513.

16. Knoppe, S.; Verbiest, T. Resonance Enhancement of Nonlinear Optical Scattering in Monolayer-Protected Gold Clusters. *J. Am. Chem. Soc.* **2017**, *139*, 14853–14856.
17. Antonello, S.; Arrigoni, G.; Dainese, T.; Nardi, M. D.; Parisio, G.; Perotti, L.; René, A.; Venzo, A.; Maran, F. Electron Transfer through 3D Monolayers on Au_{25} Clusters. *ACS Nano* **2014**, *8*, 2788–2795.
18. Templeton, A. C.; Wuelfing, W. P.; Murray, R. W. Monolayer-Protected Cluster Molecules. *Acc. Chem. Res.* **2000** *33*, 27–36.
19. Angel, L.; Majors, L.; Dharmaratne, A.; Dass, A. Ion Mobility Mass Spectrometry of $Au_{25}(SCH_2CH_2Ph)_{18}$ Nanoclusters. *ACS Nano* **2010**, *4*, 4691–4700.
20. Baksi, A.; Harvey, S. R.; Natarajan, G.; Wysocki, V. H.; Pradeep, T. Possible Isomers in Ligand Protected Ag_{11} Cluster Ions Identified by Ion Mobility Mass Spectrometry and Fragmented by Surface Induced Dissociation. *Chem. Commun.* **2016**, *52*, 3805–3808.
21. Baksi, A.; Chakraborty, P.; Bhat, S.; Natarajan, G.; Pradeep, T. Isomerism in Monolayer Protected Silver Cluster Ions: An Ion Mobility-Mass Spectrometry Approach. *Chem. Commun.* **2016**, *52*, 8397–8400.
22. Ligare, M. R.; Baker, E. S.; Laskin, J.; Johnson, G. E. Ligand Induced Structural Isomerism in Phosphine Coordinated Gold Clusters Revealed by Ion Mobility Mass Spectrometry. *Chem. Commun.* **2017**, *53*, 7389–7392.
23. Hamouda, R.; Bertorelle, F.; Rayane, D.; Antoine, R.; Broyer, M.; Dugourd, P. Glutathione Capped Gold $Au_M(SG)_M$ Clusters Studied by Isotope-Resolved Mass Spectrometry *Int. J. Mass Spectrom.* **2013**, *335*, 1–6.
24. Black, D. M.; Bhattarai, N.; Whetten, R. L.; Bach, S. B. H. Collision-Induced Dissociation of Monolayer Protected Clusters Au_{144} and Au_{130} in an Electrospray Time-of-Flight Mass Spectrometer. *J. Phys. Chem. A* **2014**, *118*, 10679–10687.
25. Johnson, G. E.; Olivares, A.; Hill, D.; Laskin, J. Cationic Gold Clusters Ligated with Differently Substituted Phosphines: Effect of Substitution on Ligand Reactivity and Binding. *Phys. Chem. Chem. Phys.* **2015**, *17*, 14636–14646.
26. Black, D. M.; Crittenden, C. M.; Brodbelt, Whetten, R. L. Ultraviolet Photodissociation of Selected Gold Clusters: Ultraefficient Unstapling and Ligand Stripping of $Au_{25}(pMBA)_{18}$ and $Au_{36}(pMBA)_{24}$. *J. Phys. Chem. Lett.* **2017**, *8*, 1283–1289.
27. Hamouda, R.; Bellina, B.; Bertorelle, F.; Compagnon, I.; Antoine, R.; Broyer, M.; Rayane, D.; Dugourd, P. Electron Emission of Gas-Phase $[Au_{25}(SG)_{18}\text{-}6H]^{7-}$ Gold Cluster and Its Action Spectroscopy. *J. Phys. Chem. Lett.* **2010**, *1*, 3189–3194.
28. Schulz-Dobrick, M.; Jansen, M. Supramolecular Intercluster Compounds Consisting of Gold Clusters and Keggin Anions. *Eur. J. Inorg. Chem.* **2006**, *2006*, 4498–4502.
29. Wen, F.; Englert, U.; Gutrath, B.; Simon, U. Crystal Structure, Electrochemical and Optical

Properties of $[Au_9(PPh_3)_8](NO_3)_3$. *Eur. J. Inorg. Chem.* **2008**, *2008*, 106–111.

30. Ito, L. N.; Johnson, B. J.; Mueting, A. M.; Pignolet, L. H. Heterobimetallic Au–Pd Phosphine Cluster Complexes. X-ray Crystal and Molecular Structure of $[Au_8Pd(PPh_3)_8](NO_3)_2$. *Inorg. Chem.* **1989**, *28*, 2026–2028.
31. Matsuo, S.; Takano, S.; Yamazoe, S.; Koyasu, K.; Tsukuda, T. Selective and High-Yield Synthesis of Oblate Superatom $[PdAu_8(PPh_3)_8]^{2+}$. *ChemElectroChem* **2016**, *3*, 1206–1211.
32. Briant, C. E.; Hall, K. P.; Mingos, D. M. P. Structural Characterisation of Two Crystalline Modifications of $[Au_9\{P(C_6H_4OMe\text{-}p)_3\}_8](NO_3)_3$: The First Example of Skeletal Isomerism in Metal Cluster Chemistry. *J. Chem. Soc., Chem. Commun.* **1984**, 290–291.
33. Yamazoe, S.; Matsuo, S.; Muramatsu, S.; Takano, S.; Nitta, K.; Tsukuda, T. Suppressing Isomerization of Phosphine-Protected Au_9 Cluster by Bond Stiffening Induced by a Single Pd Atom Substitution. *Inorg. Chem.* **2017**, *56*, 8319–8325.
34. Takano, S.; Hirai, H.; Muramatsu, S.; Tsukuda, T. Hydride-Doped Gold Superatom $(Au_9H)^{2+}$: Synthesis, Structure, and Transformation. *J. Am. Chem. Soc.* **2018**, *140*, 8380–8383.
35. Pringle, S. D.; Giles**,** K.; Wildgoose, J. L.; Williams**,** J. P.; Slade, S. E.; Thalassinos, K.; Bateman, R. H.; Bowers, M. T.; Scrivens, J. H. An Investigation of the Mobility Separation of Some Peptide and Protein Ions Using a New Hybrid Quadrupole/Travelling Wave IMS/oa-ToF Instrument. *Int. J. Mass Spectrom.* **2007**, *261*, 1–12.
36. Giles, K.; Williams, J. P.; Campuzano, I. Enhancements in Travelling Wave Ion Mobility Resolution. *Rapid Commun. Mass Spectrum.* **2011**, *25*, 1559–1566.
37. Shvartsburg, A. A.; Smith, R. D. Fundamentals of Traveling Wave Ion Mobility Spectrometry. *Anal. Chem.* **2008**, *80*, 9689–9699.
38. Bush, M. F.; Hall, Z.; Giles, K.; Hoyes, J.; Robinson, C. V.; Ruotolo B. T. Collision Cross Sections of Proteins and Their Complexes: A Calibration Framework and Database for Gas-Phase Structural Biology. *Anal. Chem.* **2010**, *82*, 9557–9565.
39. Ruotolo B. T.; Benesch, J. L.P.; Sandercock, A. M.; Hyung, S.; Robinson, C. V. Ion Mobility-Mass Spectrometry Analysis of Large Protein Complexes. *Nat. Protoc.* **2008**, *3*, 1139–1152.
40. Jurneczko, E.; Kalapothakis, J.; Campuzano, I. D. G.; Morris, M.; Barran, P. E. Effects of Drift Gas on Collision Cross Sections of a Protein Standard in Linear Drift Tube and Traveling Wave Ion Mobility Mass Spectrometry. *Anal. Chem.* **2012**, *84*, 8524–8531.
41. Larriba, C.; Hogan, C. J. Ion Mobilities in Diatomic Gases: Measurement versus Prediction with Non-Specular Scattering Models. *J. Phys. Chem. A* **2013**, *117*, 3887–3901.
42. von Helden, G. Hsu, M.; Gotts, N.; Bowers, M. T. Carbon Cluster Cations with up to 84 Atoms: Structures, Formation Mechanism, and Reactivity. *J. Phys. Chem.* **1993**, *97*, 8182–8192.
43. Shvartsburg, A. A.; Jarrold, M. F. An Exact Hard-Spheres Scattering Model for the Mobilities

of Polyatomic Ions. *Chem. Phys. Lett.* **1996**, *261*, 86–91.

44. Larriba-Andaluz, C. Hogan, C. J. Collision cross section calculations for polyatomic ions considering rotating diatomic/linear gas molecules. *J. Chem. Phys.* **2014**, *141*, 194107.

Chapter 4.

Concluding remarks

4.1 Summary of the thesis

As mentioned in Chapter 1, ligand-protected metal clusters have extended the scope of materials science owing to their size-specific unique properties. In Chapters 2 and 3, gas-phase measurements were applied to phosphine/thiolate-protected coinage metal clusters. In Chapter 2, I conducted anion photoelectron spectroscopy (PES) and photodissociation mass spectrometry (PDMS) of $[M_{25}(SR)_{18}]^-$ (M = Au, Ag). Irradiation of $[M_{25}(SR)_{18}]^-$ with a 355-nm photon dominated direct photodetachment from superatomic 1P orbitals and d orbitals localized on each coinage metal atom. The adiabatic electron affinity of $[M_{25}(SR)_{18}]^0$ and vertical detachment energy of $[M_{25}(SR)_{18}]^-$ were experimentally determined for the first time from the PE spectra recorded at 355 nm. On the contrary, irradiation of $[M_{25}(SR)_{18}]^-$ with a 266-nm photon induced indirect detachment of thermionic electrons from vibrationally excited M_{13} core. Thermionic emission has not been observed in bare Au_n/Ag_n clusters. Protection of the M_{13} core by stiff $M_2(SR)_3$ oligomers may contribute to promote internal conversion process from an electronically excited state to a vibrationally excited state by retardation of nuclear motion toward the dissociation. Gas-phase methods including anion PES and PDMS will provide a new opportunity to address intrinsic physicochemical properties and photo-processes of ligand protected metal clusters without any influence from the solvents (Figure 4.1).

In Chapter 3, I conducted ion mobility mass spectrometry of $[PdAu_8(PPh_3)_8]^{2+}$ and $[Au_9(PPh_3)_8]^{3+}$. The collision cross sections of $[PdAu_8(PPh_3)_8]^{2+}$ and $[Au_9(PPh_3)_8]^{3+}$ were determined by IMMS. With the reduction of the He flow rates, $[PdAu_8(PPh_3)_8]^{2+}$ and $[Au_9(PPh_3)_8]^{3+}$ underwent collision-induced isomerization to smaller species with the CCS values of 404 and 402 $Å^2$, respectively. This experimental observation illustrates the conversion of the clusters with disordered ligand layers in the solution into their single-

crystal structures with packed ligand layers. IMMS will be helpful for structural characterization in ligand-protected metal clusters in dispersion and for understanding their isomerization processes in the gas phase (Figure 4.1).

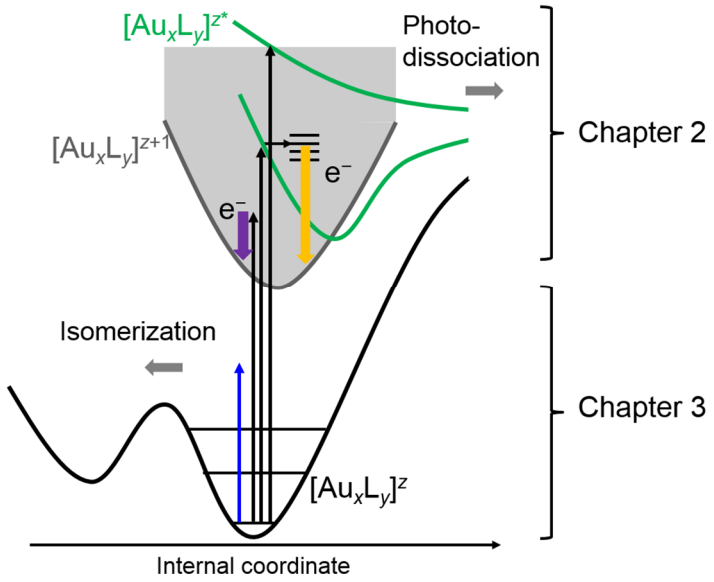

Figure 4.1 Summary of the thesis. Black and blue arrows indicate photoexcitation and collisional excitation, respectively. Orange and purple arrows correspond to direct and indirect photodetachment process, respectively.

4.2 Future prospects

In this thesis, I demonstrated the potential of gas-phase measurements for in-depth characterization of chemically-modified coinage metal clusters that can be viewed as chemically-modified superatoms.[1] I observed a new photophysical phenomenon in ligand-protected Au clusters such as thermionic emission by eliminating the perturbation from surrounding environment. I also succeeded in determining the electron binding energies of $[M_{25}(SR)_{18}]^-$ having the icosahedral Au_{13} core with eight electrons. These results quantitatively deepen our fundamental understanding for intrinsic

physicochemical properties. However, the effects of the core volume and heteroatom doping on the energy levels of superatomic orbitals have not yet been addressed. These question can be addressed by expanding the targets to selenolate-protected Au clusters such as $[Au_{25}(SeR)_{18}]^{-}$,[2] thiolate-protected alloy clusters such as $[Ag_nAu_{25-n}(SR)_{18}]^{-}$,[3] and thiolate-protected Ag and Ag-based alloy clusters including $[Ag_{25}(SR)_{18}]^{-}$,[4] $[AuAg_{24}(SR)_{18}]^{-}$,[5] $[MAg_{24}(SR)_{18}]^{2-}$ (M = Pt, Pd),[6] $[Ag_{29}(S_2R)_{12}]^{3-}$,[7] and $[Ag_{44}(SR)_{30}]^{4-}$.[8] All the clusters mentioned here have an icosahedral M_{13} (M = Au, Ag), doped MAg_{12} (M = Pt, Pd), or Ag_mAu_{13-m} core protected by ligands. These protected clusters are suitable platforms to study modulation of electronic structure of the core by substituting the central atoms and changing the electron withdrawing ability, composition, and charge state of protecting ligands without any other additional perturbations. For example, $[MAg_{24}(SPhMe_2)_{18}]^{2-}$ (M = Pt, Pd) has the same protecting oligomer motif, L_1^{-} (= $Ag_2(SPhMe_2)_3^{-}$), as $[Ag_{25}(SPhMe_2)_{18}]^{-}$, while it has the different MAg_{12} core (Figure 4.2). In contrast, $[Ag_{29}(S_2C_6H_4)_{12}]^{3-}$ has the same Ag_{13} core, while it has the more negatively charged ligand layer, L_2^{2-} (= $Ag_4(S_2C_6H_4)_3^{2-}$), than those of $[Ag_{25}(SR)_{18}]^{-}$ (Figure 4.2). Anion PES will allow us to investigate the intrinsic electronic structures of these chemically-synthesized Ag clusters and the effect of core motif or ligand motif on the electronic structure.

The results of IMMS revealed that the structures of the ligand layers of $[PdAu_8(PPh_3)_8]^{2+}$ and $[Au_9(PPh_3)_8]^{3+}$ in dispersion were retained during desolvation via electrospray ionization (ESI). This shows the new possibility of exploring the geometric structure in dispersion and the isomerization process including ligand layers by ESI IMMS.

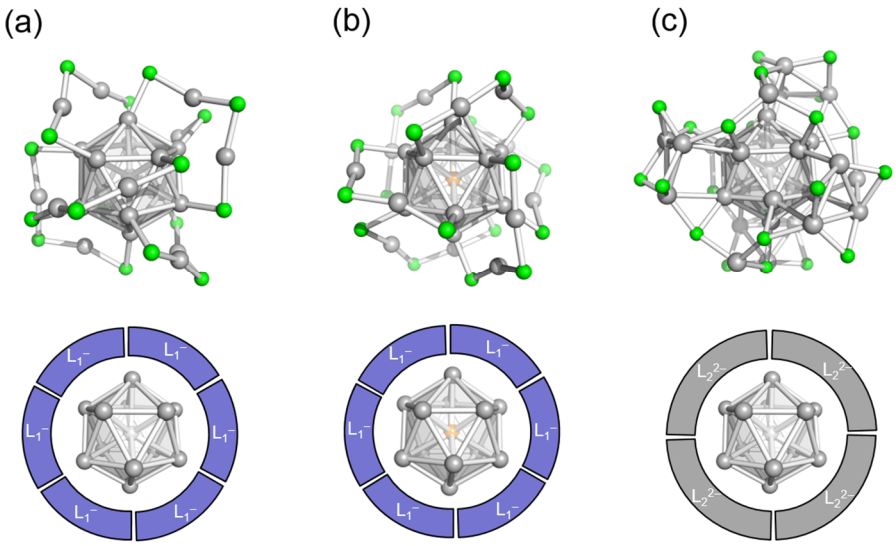

Figure 4.2 Crystal structures and conceptual illustrations of geometric structures of (a) $[Ag_{25}(SR)_{18}]^{-}$, (b) $[MAg_{24}(SR)_{18}]^{2-}$, and (c) $[Ag_{29}(S_2R)_{12}]^{3-}$.

References

1. Walter, M.; Akola, J.; Lopez-Acevedo, O.; Jadzinsky, P. D.; Calero, G.; Ackerson, C. J.; Whetten, R. L.; Grönbeck, H.; Häkkinen, H. A Unified View of Ligand-Protected Gold Clusters as Superatom Complexes. *Proc. Natl. Acad. Sci.* **2008**, *105*, 9157–9162.
2. Negishi, Y.; Kurashige, W.; Kamimura, U. Isolation and Structural Characterization of an Octaselenolate-Protected Au_{25} Cluster. *Langmuir* **2011**, *27*, 12289–12292.
3. Negishi, Y.; Iwai, T.; Ide, M. Continuous Modulation of Electronic Structure of Stable Thiolate-Protected Au_{25} Cluster by Ag Doping. *Chem. Commun.* **2010**, *46*, 4713–4715.
4. Joshi, C. P.; Bootharaju, M. S.; Alhilaly, M. J.; Bakr, O. M. $[Ag_{25}(SR)_{18}]^-$: The "Golden" Silver Nanoparticle. *J. Am. Chem. Soc.* **2015**, *137*, 11578–11581.
5. Bootharaju, M. S.; Sinatra, L.; Bakr, O. M. Distinct Metal-Exchange Pathways of Doped Ag_{25} Nanoclusters. *Nanoscale* **2016**, *8*, 17333–17339.
6. Yan, J.; Su, H.; Yang, H.; Malola, S.; Lin, S.; Häkkinen, H.; Zheng, N. Total Structure and Electronic Structure Analysis of Doped Thiolated Silver $[MAg_{24}(SR)_{18}]^{2-}$ (M =Pd, Pt) Clusters. *J. Am. Chem. Soc.* **2015**, *137*, 11880–11883.
7. AbdulHalim, L. G.; Bootharaju, M. S.; Tang, Q.; Del Gobbo, S.; AbdulHalim, R. G.; Eddaoudi, M.; Jiang, D.-e.; Bakr, O. M. $Ag_{29}(BDT)_{12}(TPP)_4$: A Tetravalent Nanocluster. *Nanoscale* **2016**, *8*, 17333–17339.
8. Desireddy, A.; Conn, B. E.; Guo, J.; Yoon, B.; Barnett, R. N.; Monahan, B. M.; Kirschbaum, K.; Griffith, W. P.; Whetten, R. L.; Landman, U.; Bigioni, T. Ultrastable Silver Nanoparticles. *Nature* **2013**, *501*, 399–402.

List of publications and presentations

Publications related to the thesis

(Chapter 2)

1. "Anion Photoelectron Spectroscopy of Free $[Au_{25}(SC_{12}H_{25})_{18}]^-$", Keisuke Hirata, Keishiro Yamashita, Satoru Muramatsu, Shinjiro Takano, Keijiro Ohshimo, Toshiyuki Azuma, Ryuzo Nakanishi, Takashi Nagata, Seiji Yamazoe, Kiichirou Koyasu and Tatsuya Tsukuda, *Nanoscale* **2017**, *9*, 13409–13412.
2. "Photo-Induced Thermionic Emission from $[M_{25}(SR)_{18}]^-$ (M = Au, Ag) Revealed by Anion Photoelectron Spectroscopy", Keisuke Hirata, Kuenhee Kim, Katsunosuke Nakamura, Hirokazu Kitazawa, Shun Hayashi, Kiichirou Koyasu and Tatsuya Tsukuda, *J. Phys. Chem. C* submitted.

(Chapter 3)

3. "Interconversions of Structural Isomers of $[PdAu_8(PPh_3)_8]^{2+}$ and $[Au_9(PPh_3)_8]^{3+}$ Revealed by Ion Mobility Mass Spectrometry", Keisuke Hirata, Papri Chakraborty, Abhijit Nag, Shinjiro Takano, Kiichirou Koyasu, Thalappil Pradeep and Tatsuya Tsukuda, *J. Phys. Chem. C* **2018**, *122*, 23123–23128.

Publication not related to the thesis

1. "Collision-Induced Dissociation of Undecagold Clusters Protected by Mixed Ligands $[Au_{11}(PPh_3)_8X_2]^+$ (X = Cl, C≡CPh)", Ryohei Tomihara, Keisuke Hirata, Hiroki Yamamoto, Shinjiro Takano, Kiichirou Koyasu, and Tatsuya Tsukuda, *ACS Omega* **2018**, *3*, 6237–6242.

Oral Presentations

1. “Gas-Phase Photoelectron Spectroscopy on Thiolate-Protected Coinage Metal Clusters (I): Photo-Induced Thermionic Emission”, Keisuke Hirata, Kuenhee Kim, Katsunosuke Nakamura, Shinjiro Takano, Kiichirou Koyasu, and Tatsuya Tsukuda The 99th CSJ Annual Meeting, Okamoto Campus, Konan University, Kobe, March 2019.
2. “Isomerization of $[PdAu_8(PPh_3)_8]^{2+}$ in the Gas Phase”, Keisuke Hirata, Satoru Muramatsu, Papri Chakraborty, Abhijit Nag, Shinjiro Takano, Kiichirou Koyasu, Tatsuya Tsukuda and Thalappil Pradeep, The 98th CSJ Annual Meeting, Funabashi Campus, Nihon University, Funabashi, March 2018.
3. “負イオン光電子分光による配位子保護金属クラスターの超原子軌道の直接観測”, 平田圭祐, 山下恵史朗, 村松悟, 高野慎二郎, 大下慶次郎, 東俊行, 中西隆造, 永田敬, 山添誠司, 小安喜一郎, 佃達哉, 第 11 回分子科学討論会, 東北大学川内北キャンパス, 仙台, 2017 年 9 月.
4. “Anion Photoelectron Spectroscopy of Free Thiolate-Protected Metal Clusters”, Keisuke Hirata, Keishiro Yamashita, Satoru Muramatsu, Shinjiro Takano, Seiji Yamazoe, Kiichirou Koyasu and Tatsuya Tsukuda, International Symposium on Monolayer-Protected Clusters, Monte Verità, Ascona, Switzerland, August 2017.
5. “Anion Photoelectron Spectroscopy of Thiolate-Protected Au_{25} Clusters in Gas Phase”, Keisuke Hirata, Satoru Muramatsu, Keishiro Yamashita, Shinjiro Takano, Seiji Yamazoe, Kiichirou Koyasu and Tatsuya Tsukuda, The 97th CSJ Annual Meeting, Hiyoshi Campus, Keio University, Yokohama, March 2017.
6. “チオラート保護金属クラスターの表面誘起解離質量分析”, 平田圭祐, 高野慎二郎, 江守宗次郎, 北澤啓和, 山添誠司, 小安喜一郎, 佃達哉, 第 10 回分子科学討論会, 神戸ファッションマート, 神戸, 2016 年 9 月.

Poster Presentations

1. "Ion Mobility Mass Spectrometry on $[PdAu_8(PPh_3)_8]^{2+}$ and $[Au_9(PPh_3)_8]^{3+}$", Keisuke Hirata, Papri Chakraborty, Abhijit Nag, Shinjiro Takano, Kiichirou Koyasu, Thalappil Pradeep, and Tatsuya Tsukuda, Asian Symposium on Nanoscience and Nanotechnology, Takeda Building, University of Tokyo, Tokyo, May 2018.
2. "Surface-Induced Dissociation of $Au_{25}(SR)_{18}^-$ and $Ag_{25}(SR)_{18}^-$ Cluster Anions", Keisuke Hirata, Shinjiro Takano, Sojiro Emori, Seiji Yamazoe, Kiichirou Koyasu, and Tatsuya Tsukuda, The 24th ZESTY Seminar, Chemistry Building, University of Tokyo, Tokyo, February 2017.
3. "チオラート保護金属クラスターの表面誘起解離", 平田圭祐, 高野慎二郎, 江守宗次郎, 北澤啓和, 山添誠司, 小安喜一郎, 佃達哉, ナノ学会第 14 回大会, 北九州国際会議場, 北九州, 2016 年 6 月.
4. "Surface-Induced Dissociation of Thiolate-Protected Metal Clusters", Keisuke Hirata, Shinjiro Takano, Sojiro Emori, Seiji Yamazoe, Kiichirou Koyasu, and Tatsuya Tsukuda, Cluster Surface Interaction Workshop 2016, Argonne National Laboratory, IL, the U.S., May 2016.

Acknowledgments

The works in the thesis were conducted during my Ph. D. course in Department of Chemistry, Graduate School of Science, the University of Tokyo, under the supervision of Prof. Tatsuya Tsukuda. I deeply appreciate Prof. Tatsuya Tsukuda for his instructions, scientific discussions and encouragements for six years. I also thank him for giving me an opportunity to enrich my understanding of chemistry and science and to discuss scientific issues with a lot of peoples. I give my gratitude to Associate Prof. Kiichirou Koyasu for his expert advice on gas-phase measurements and discussions on weekly seminars. I sincerely thank Assistant Prof. Shinjiro Takano for synthesis of chemically-modified Au clusters. I am indebted to Ms. Yuka Sakurai for her support in every office work.

I dedicate my gratitude to former staff members of Tsukuda laboratory. I thank Prof. Seiji Yamazoe (Graduate School of Science and Engineering, Tokyo Metropolitan University) for his inspiring instructions from the perspective of synchrotron radiation. I am grateful to Assistant Prof. Satoru Muramatsu (Graduate School of Science, Hiroshima University) for the daily talks and discussion.

I am grateful to all the current members of Tsukuda Laboratory: Dr. Liang Feng, Mr. Ryohei Tomihara, Mr. Shun Hayashi, Mr. Sojiro Emori, Mr. Kazuyuki Tsuruoka, Mr. Tsubasa Omoda, Mr. Naoaki Shinjo, Mr. Yuto Nakajima, Mr. Shingo Hasegawa, Mr. Rei Horie, Mr. Shunichi Yamazaki, Mr. Kuenhee Kim, Mr. Wei Loon Lim, Mr. Satoshi Osugi, Mr Takeki Konuma, Ms. Megumi Suyama, Mr. Katsunosuke Nakamura, Mr. Haru Hirai, Mr. Atsushi Matsuo, Mr. Mizuki Shimojima, Mr. Shun Ito, Mr. Taro Shigeta, and Ms. Koto Hirano.

I thank former members of Tsukuda Laboratory: Dr. Ryo Takahata, Mr. Naoto Sasaki, Mr. Daiki, Shuto, Mr. Toshiaki Yanase, Mr. Hiroki Yamada, Mr. Hiroki Yamamoto, Dr. Hirokazu Kitazawa, Mr. Ryo Ishida, Mr. Keishiro Yamashita, Mr. Ryota Shibuya, Mr. Akimaro

Yanagimachi, Mr. Shota Matsuo, Mr. Teppei Misumi, Mr. Tatsuya Higaki, Dr. Tomomi Watanabe, Ms. Setsuka Arii, Mr. Masaru Urushizaki, Mr. Yuichiro Kawahara, Dr. Md. Jafar Sharif, Dr. Junichi Nishigaki, and Ms. Nana Kawada.

This thesis contains the collaborative works. I would like to address special thanks to all the collaborators. I deeply thank Dr. Takashi Nagata (SOKENDAI) and Dr. Ryuzo Nakanishi (QST) for installing the photoelectron analyzer. I am sincerely helpful to Dr. Toshiyuki Azuma (RIKEN) and Asscociate Prof. Keijiro Ohshimo (Graduate School of Science, Tohoku University) for photodissciation mass spectrometry of $[Au_{25}(SR)_{18}]^-$. I appreciate Prof. T. Pradeep (Indian Institute of Technology Madras) for giving me an opportunity to use the ion mobility mass spectrometer (IMMS). He also gave me precious advice both on scientific discussion and on daily life in India. I thank all the members in Pradeep's laboratory for kindly accepting me. Especially I thank Ms. Papri Chakraborty and Mr. Abhijit Nag, who are the coauthors of the article on IMMS of $[PdAu_8(PPh_3)_8]^{2+}$ and $[Au_9(PPh_3)_8]^{3+}$.

I was adopted as a member of Materials Education Program for the Future Leaders in Research, Industry, and Technology (MERIT), which is a leading program in the University of Tokyo. I deeply thank MERIT for providing me with fruitful seminars and financial support. I address my special thanks to my subsupervisor Prof. Takahisa Arima (Graduate School of Frontier Sciences, the University of Tokyo) for precious advice.

December 2018

Keisuke Hirata